Università degli Studi di Padova

Dipartimento di Fisica e Astronomia "Galileo Galilei"

Corso di Laurea Magistrale in Astronomia

Compensation of Non Common Path Aberrations on a pyramid wavefront sensor with an Adaptive Lens

Compensazione delle aberrazioni su un cammino non comune con una lente adattiva su un sensore di fronte d'onda a piramide

Laureando

Paolo Favazza

Relatore

Prof. Mauro D'Onofrio

Co-relatori

Prof. Stefano Bonora
Prof. Demetrio Magrin
Dott. Martino Quintavalla
Dott.ssa Maria Bergomi

ii

Contents

Abstract

Closed loop systems based on the Pyramid wavefront sensor (P-WFS) can reach very high sensitivity respect to other wavefront sensors. The sensitivity increases as the Point Spread Function (PSF) on the tip of the pyramid gets smaller. Therefore, it is very important that in closed loop systems operating with the P-WFS the Non common Path Aberrations (NCPA) between the scientific camera arm and the P-WFS arm are reduced as much as possible. This thesis aims to study the performances of the reduction of NCPA using a multi-actuator deformable lens.

Starting from the analytic simulations of the sensitivity gain of the P-WFS, mainly conducted by Ragazzoni, Verinuad and Viotto, I developed an AO system to show experimentally the magnitude gain due to the P-WFS with respect to a Shack-Hartmann wavefront sensor (SH-WFS) when the sensitivity of the P-WFS increases with the decreasing of the aberrations. In fact, the P-WFS has the intrinsic capability to increase the gain as the aberrations are reduced; differently the SH-WFS maintains a constant gain under the same conditions. The most remarkable consequence is an improvement of the magnitude limit of observable stars with closed loop adaptive optics system. This is the feature of the P-WFS, that has made it the most implemented wavefront sensor in astronomic field in the last decade.

Moreover, the multi-actuator deformable lens, recently developed at CNR-IFN of Padua, is a promising device already used, with great results, in microscopy and ophthalmic instruments field. This adaptive lens has the unique feature of correcting aberrations up to the 4th order such as a deformable mirror allowing the realization of very compact optical setup. In particular, I have used the deformable lens (DL) to correct the non common path aberrations in closed loop mode between a P-WFS and a SH-WFS. The results show that the multi-actuator adaptive lens can be used to reduce the NCPA very close to the diffraction limit and that the correction can be maintained over a medium term operation with good stability.

Chapter 1

Introduction

Adaptive Optics (AO) is a technology developed to correct in real time the aberrations that occur when light propagates through an inhomogeneous medium. Nowadays, AO is implemented in astronomy, in military applications (Tyson, 2001, [1]) and in microscopy, especially for medical purposes (Bonora, 2015, [2]). The designing and the building of the AO system requires knowledge from many fields: astronomy, optics, electrical and mechanical engineering, computer science and control theory. The first idea of AO was mentioned in 1950s. However, it was not developed until 1970s, when the technologies become sufficiently sophisticated through the implementation in military field (Hardy, 1998, [3]). In Astronomy, the first successful AO systems were used in the larger telescopes at the beginning of the 1990s. The light coming from a distant and unresolved astronomical source forms a wavefront (WF) that can be considered plane just outside of the atmosphere. When it propagates through the atmosphere, the variation of the refractive index of air cause the deformation of the wavefront shape. The device measuring these deformations is called a wavefront sensor (WFS). Currently the principal AO solutions are based on closed loop WFS: the incoming light is reflected from a deformable optical element, then it is divided in two parts. The first part is directed to a scientific camera, while the other to the WFS. The sensor measures the wavefront deformations and these measurements are sent to a control unit that computes the commands to send to the deformable element. The deformable optical element, through these commands, changes its shape to correct the wavefront. This process thus compensates the atmospheric turbulence eliminating the deformations of the wavefront.

The first generation AO systems was designed to be used with a single deformable optical element and a single WFS; it has called Single Conjugate Adaptive Optics (SCAO). These systems are able to compensate only a small field of view around the reference star (up to a few tens of arcseconds at near

infrared). The first wavefront sensors were obtained by the classical devices used in optical testing (Hardy, 1998, [3]). It was the Shack-Hartmann WFS that separates the light of the pupil over several sub-apertures and measures the local derivative of the wavefront inside of them. However the SH-WFS has some fundamental features making its use in some applications less efficient, especially with the next generation large telescopes. In fact, to reach a good spatial resolution with SH-WFS, the incoming wavefront has to be split into several independent images. More independent images are formed and more deeply is the sampling of the wavefront, but, in this way, each sub-aperture receives lesser amount of photons increasing the Poisson errors on the measurements. Moreover, the sensitivity of the SH-WFS depends on the diameter of the sub-apertures and so it is fixed. Therefore, the system must reach a compromise between high spatial sampling and high accuracy of measurements (Verinaud, 2005, [4]).

Other WFSs have been presented and implemented up today; among these, there is the P-WFS (Ragazzoni, 1996, [5]). At the moment it is the widely used in astronomy due to the fact that it presents a better sensitivity compared to SH-WFS. All theoretical studies (Ragazzoni, 2002, [6]), numerical analyzes (Lee, 2000, [7]; Verinaud, 2003, [8]; Verinaud, 2005, [4]; Louarn, 2005, [9]) and practical experiments (Ragazzoni, Diolaiti, Vernet, 2000, [10]; Wang, 2011, [11]; Yong Liu, 2017, [12]) have demonstrated the P-WFS advantages over SH-WFS, especially to measure the wavefront deformations of faint sources as in astronomy. One disadvantage of the P-WFS is however its small linearity range. If the measured wavefront deformations are too large, the sensor saturates and its response is no more linear.

This thesis focus on the correction of non common path aberrations with a deformable lens. In a typical astronomical instrument with an AO system, the light is separated between the scientific arm and the WFS arm. After this separation, the light follows different paths, i.e. differential aberrations. When the loop is closed, thus the aberrations are eliminated in the WFS arm, these NCPA affects the scientific images. In general, a bias corresponding to the NCPA is introduced on the WFS measurement in order to achieve a diffraction limited image on the scientific camera. However, in the case of P-WFS this correction diminishes its gain and then its sensitivity. Indeed, the sensitivity of the P-WFS depends on strength of the aberrations, i.e. stronger are the aberrations and smaller is the sensitivity of the P-WFS. The next Chapters explain as a deformable lens allows to correct the non common path aberrations of the system. In this way, the P-WFS reaches its maximum sensitivity value without introducing any NCPA in the scientific arm. The increasing of the sensitivity of the P-WFS permits to measure and to correct smaller aberrations or, alternately, to use fainter sources (Viotto,

2016, [13]). This is the focal point of this thesis. To do this, a SH-WFS is used as "scientific camera" of the AO system and it evaluates the non common path aberration of the P-WFS system in closed loop with respect the SH-WFS arm. Then a DL is used to correct the NCPA and to evaluate the sensitivity gain of the P-WFS. In the following the contents of the thesis are briefly summarized.

The Chapter 2 introduces some concepts related with the aberration of the light. In particular what causes the deformation of the wavefront and how we can study the spatial and temporal variations of these aberrations. Here it reports the treatment of Kolmogorov to model the turbulence of the air and the Zernike polynomials that allow to describe the wavefront shape.

The Chapter 3 explains the main components and the functioning of AO systems. In particular, it dwell on the comparison between the pyramid sensor and the Shack-Hartmann sensor. Moreover this Chapter explains the features of the deformable lens.

The Chapter 4 describes the experimental system, in particular, how it has been implemented and how it works. Moreover this Chapter explains the calibration method used to calibrate the AO system and how the data have acquired. Finally, it describes the stability of the system and the measurements of the NCPA.

The Chapter 5 demonstrates the improvement of the sensitivity in the P-WFS when the NCPA are reduced or eliminated. Then, it calculates the theoretical magnitude gain of the system without NPCA starting from the theoretical curves of magnitude gain for the P-WFS. Finally, this Chapter concludes the thesis with discussion of the collected data. In particular, it discusses the utility of the deformable lens in astronomic field.

Chapter 2

The optical aberrations

In the last century the technological development has brought the possibility to build more sophisticated devices. Particularly, in the astronomic field it has been possible to build larger telescopes, which have higher resolution limit, and equipments able to measure sources more distant and fainter. The limit of resolution of a perfect optical system is the diffraction limit. The resolution is the ability to distinguish two points separated by a certain angle with respect to the observer. In fact, according to the formulation of Airy, a point source is brought on an image plane through an optical system. Here the image of the point source is not a point but a spot, in particular a point spread function (PSF). This physical phenomenon is due to the limitation imposed by the finite collecting area of the telescope and by the undulated nature of the light. Both of them lead to the impossibility to make a point image of a point source. The size of the spot, assuming a circular entrance pupil, can be obtained by the equation of Airy:

$$d = 1.22 \frac{\lambda}{D} f \qquad (2.1)$$

where d is the size of the spot, λ the wavelength of the observation, D is the diameter of the aperture of our system and f is its focal length. From this equation we can immediately deduce that, if the diameter of the system increases, the instrument is able to resolve closer points on the object plane (Cheng, 2009, [14]). This property and the possibility to accumulate more photons have brought the astronomers to build larger telescopes.

Unfortunately, the turbulence of the atmosphere limits the resolution of the large ground telescopes. In fact, Airy size can be reached only for unaberrated wavefront, typically in absence of turbulence or for diameters of telescopes smaller than the characteristic parameter of the turbulence r_0. In particular, the atmospheric turbulence can be modeled as it was composed

by portions with constant phase having size typically larger than $r_0 \approx 20 \; cm$ (McKechnie, 2016, [15]). Therefore, the size of this portion becomes the new aperture limit for the larger telescopes.

$$d = 1.22 \frac{\lambda}{r_0} f \qquad (2.2)$$

For example, the telescope $E - ELT$ planned by ESO (European Southern Observatory) is a 40m-class; it has the same resolution of the Galileo telescope in Asiago (1.2 m), but only if there is any AO system implemented on both. The difference consists in the amount of photons captured by the telescopes.

This limitation can be mitigated by introducing the Adaptive Optics System. This technique allows to measure the deformations acquired by the wavefront through the atmospheric turbulence. Subsequently, using a deformable optical element, it is possible to recover the unperturbed wavefront by applying the opposite deformation. Therefore the resolution of the telescope tends to own diffraction limit. In figure 2.1 is shown a scheme of classic optical system with AO in closed loop.
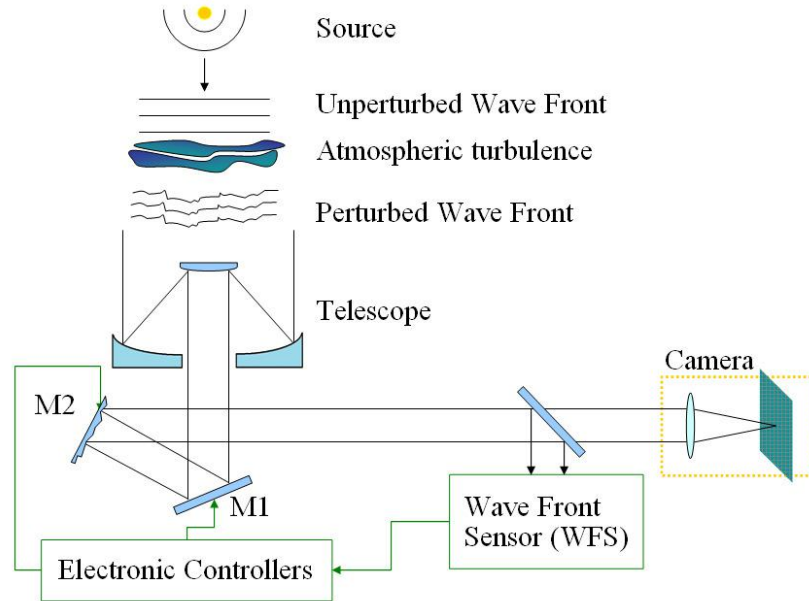

Figure 2.1: Pattern of a telescope equipped with a classic AO system in closed loop with M1 and M2 the deformable optical elements.

A wavefront, coming from an astronomical source, is perturbed by the atmospheric turbulence and it is collected by a telescope. The wavefront

reaches the deformable optical elements $M1$ and $M2$ and then it is divided in two portions. A portion goes to the scientific camera and the other goes to the WFS. Here the computer measures the aberrations of the wavefront and it computes the deformation to send to the deformable elements to correct the wavefront. Thanks to the adaptive optics, a ground telescope should observe an astronomical object as if it were in absence of the atmospheric turbulence. Therefore a perfect AO is able to bring the resolution of the telescope to the theoretical one.

2.1 Atmospheric turbulence

The ability to observe the light coming from an astronomical object depends mainly on the features of the object (brightness, apparent dimension, etc.) and on the characteristics of the used tool (eye, telescope, etc.). But there is another fundamental component: the medium interposed between the source and the observer. In astronomy and in microscopy the medium between observer and source can become the most important component for the quality of the image. In astronomy the medium consists of the atmospheric layers of the Earth (obviously for ground telescopes). In microscopy it is composed by the stratification of the sample. In both cases the medium causes aberrations of the wavefront and loss of resolution of the image.

The principal feature of medium, which determines the transmission of the electromagnetic waves, is the refractive index. In the air the value of the refractive index depends on the considered wavelength, on the temperature and on the pressure of the air, according to the following equation taken by the treatment of Chauchy:

$$n - 1 = \frac{77 \cdot 10^{-6}}{T} \left(1 + 7.52 \cdot 10^{-3} \cdot \lambda^{-2}\right) \left(P + 4810\frac{p}{T}\right) \qquad (2.3)$$

where T is temperature in Kelvin, P is pressure in *mbar* and p is the pressure of the water vapor. Another simpler equation was obtained by Gladstone as:

$$n - 1 = 77 \cdot 10^{-6} \cdot \frac{P}{T} \qquad (2.4)$$

In a static case, i.e. in absence of motion of air masses, the refractive index changes vertically due to the gradients of temperature and pressure. This determines a stratification of the atmosphere in which the refractive index differs among adjacent layers, but it can be considered locally constant. This is the laminar regime. If this was the real situation, it would be very easy to correct the effect caused by the atmosphere on the image. In fact, the

refractive index would be constant in time and easy to derive for every layer. Unfortunately, the turbulent motion of the atmosphere (turbulent regime) leads to mix the atmospheric layers causing continuous changing of refractive index.

2.1.1   Kolmogorov's treatment of the atmosphere

To study the deformations caused by the atmosphere to the wavefront, we must have a model that is able to describe how the turbulence is spread through space and time (Roddier, 1981, [16]; Zilitinkevich, 2008, [17]; Morris, 2015, [18]). The model more used for the atmospheric turbulence was formulated by A. N. Kolmogorov in 1941 (Tyson, 2012, [19]). This model considers the air in a thermodynamic state of turbulent regime. In fact, a fluid flow with different speed can have two kinds of regimes: the laminar regime or the turbulent regime. In the first regime the layers of fluid with different speed flow among them without mixing. While in the second regime the layers with different speed are mixed in vortexes and they dissipate their energy through friction. The separation between the two regimes depends on the Reynolds number defined as in the following equation:

$$Re(L) = \frac{L \cdot v_L}{\nu} \tag{2.5}$$

where L is the size of the vortex, v_L is the characteristic speed of the fluid and ν is the viscosity. For the characteristic values of the air we get a number of Reynolds around 10^6. It is much higher of the maximum value for a laminar regime $Re \approx 2000$. Therefore we can consider the atmosphere in a continuous turbulent motion.

Now we define two characteristic scales: L_0 (external cutoff), the size of the vortex when it is formed, and l_0 (internal cutoff), the size of the vortex when the strength of friction becomes dominant. In the atmospheric case the vortexes are created with a size of the external cutoff around some hundreds of meters (McKechnie, 2016, [15]). Then, they break in smaller vortexes up to $1 - 10$ mm (internal cutoff) where the strength of friction is sufficiently strong to destroy them. This happen inside the inertial range (see Fig. 2.2). The energy of the vortex is proportional to its size as:

$$E_k \propto K^{-5/3} \tag{2.6}$$

where $K = (2\pi)/L$ with L size of the vortex. The dimensions of the vortexes depend on the site that we are considering and on the height of the layers.

Other two fundamental parameters are the structural parameters. The first parameter, the temperature structural parameter, C_T^2 depends on the
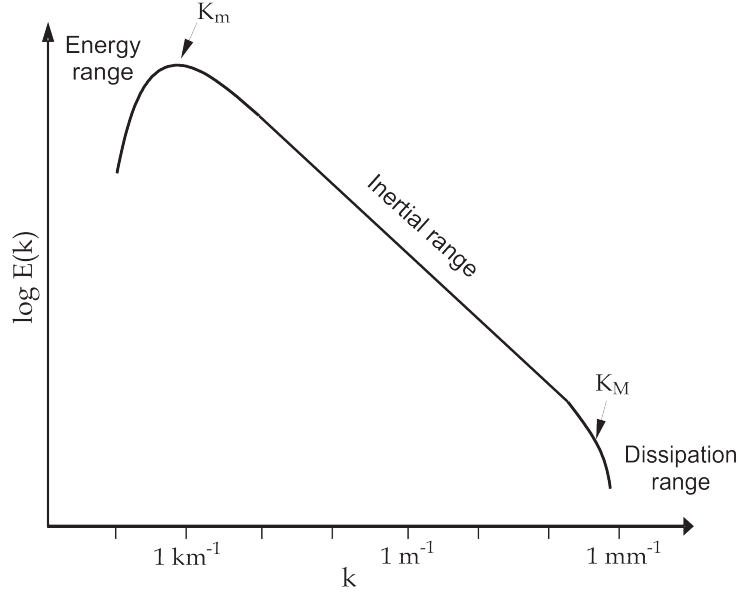
Figure 2.2: Power spectrum of the energy to be associated to the vortex in the turbulent regime. The inertial range between the internal and external scales behaves as predicted by the Kolmogorov's law. $K_m = (2\pi)/L_0$ e $K_M = (2\pi)/l_0$.

statistical variance of the temperature difference between two points. In determinate site and at specific height from the ground it is defined as:

$$C_T^2 = \sigma_{\Delta T}^2 / r^{2/3} \tag{2.7}$$

where r is the distance between two considered points along the mean wind speed and $\sigma_{\Delta T}$ is the statistical variance of the temperature. The second parameter is the refractive index structural parameter. It depends on refractive index gradient and on the temperature structural parameter as:

$$C_n^2 = \frac{\partial n}{\partial T} \cdot C_T^2 = \left(77 \cdot 10^{-6} \frac{P}{T^2}\right)^2 \cdot C_T^2 \tag{2.8}$$

With these parameters it is possible to model the effect of atmospheric turbulence on the wavefront with respect to the site considered and to the height of turbulent layers. Typically C_n^2 decreases with the height and it can present some peaks as shown in figure 2.3. In general the atmosphere can be divided in three layers (Viotto, 2012, [20]). The ground-layer has the larger value of structural parameter due to the strong gradient of temperature near the surface of Earth. It is caused by heat of soil accumulated during the day.
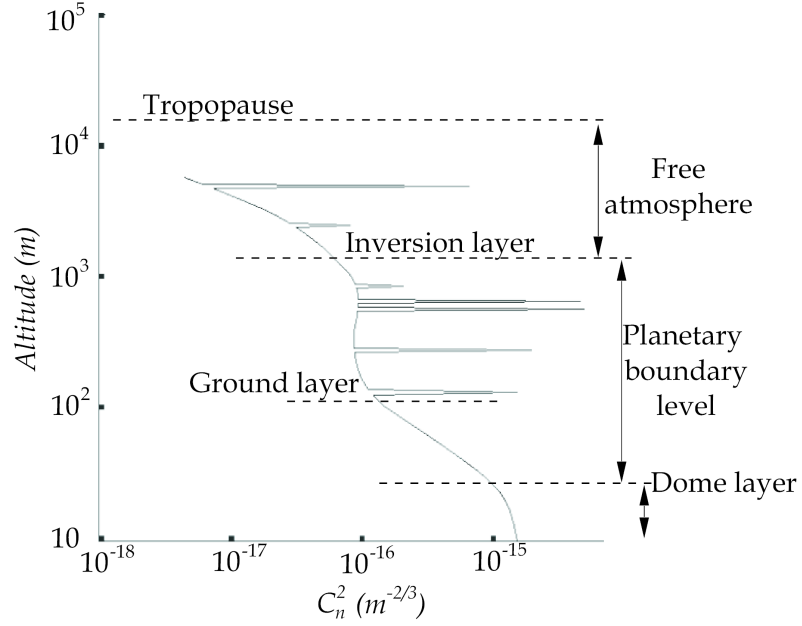
Figure 2.3: Example of vertical behavior of the atmosphere structure parameter.

Up to 1 Km there is the planetary boundary layer that produces the most aberrations of the wavefront for astronomical observation. It is due to the flow of hot air from surface layer to the free atmosphere. The last layer is the free atmosphere where the thin air leads to decrease of structural parameter and so the turbulence's strength. The structural parameters can be obtained through measurements of specific instrumentation such as balloons that map the atmosphere layers on specified sites.

2.1.2   Seeing parameters

To describe the degradation of astronomical image due to the effect of the atmosphere, we have to introduce some other parameters. The most important is the Fried parameter r_0 (Tyson, 2001, [1]). It corresponds to the length scale into which the wavefront statistically changes less than one radian:

$$r_0 = \left[0.43 \frac{4\pi^2}{\lambda^2} (\cos \phi)^{-1} \int_0^{\inf} C_n^2(z) dz \right]^{-3/5} \propto \lambda^{6/5} \qquad (2.9)$$

where ϕ is the zenith angular distance between the normal to Earth's surface and the observed direction, λ is the wavelength and C_n^2 is the refractive

index structural parameter from Kolmogorov's model. Fried's parameter can be interpreted as the size of air bubble into which the refractive index does not change significantly. It defines also the maximum resolution value of the telescope without AO system. If the telescope has the diameter much larger than r_0, we obtain in the plane image a number of spots equal to number of times Fried's parameter divides the diameter of the telescope. These spots are named speckles. They have a typical size of λ/D, but their envelop has a size of λ/r_0; namely the seeing size. When r_0 increases, the seeing decreases; increasing the wavelength the seeing decreases. A typical value of r_0 is 20 cm in the K band (McKechnie, 2016, [15]).

The second important parameter to study the aberrations of the wavefront is the isoplanatic angle θ_0. It is the angle subtended by the field of view (FoV) into which the wavefront phase statistically changes less than one radian:

$$\theta_0 = 0.314\frac{r_0}{\overline{h}} \propto \lambda^{6/5} \qquad (2.10)$$

where $\overline{h}$ is the mean height of turbulent layers. This angle corresponds to the FoV into which the perturbation introduced by the atmosphere affects the wavefront has small variations. Its typical value is a few arcseconds. This parameter provides the size of the FoV around the reference source where the wavefront is affected by the same aberrations measured from the reference source.

The last important parameter is the coherence time τ_0, i.e. the typical timescale into which the wavefront phase changes of one radian. It corresponds to the time period into which the wavefront can be considered roughly constant inside the isoplanatic patch:

$$\tau_0 = \frac{r_0}{v} \propto \lambda^{6/5} \qquad (2.11)$$

where v is the mean wind speed at the altitude of the turbulence. The coherence time is usually some tens of milliseconds in the IR domain. Like the others atmospheric parameters introduced above, it depends on the site and the considered turbulent layers. The inverse of τ_0 corresponds to the Greenwood frequency, $f_G = \tau_0^{-1} = v/r_0$. Any AO system must correct the wavefront aberrations with a frequency higher than the Greenwood frequency. In this way, the corrections are applied to a wavefront with the same aberrations.

The wavefront aberrations generate scintillation, image motion and deformations on the telescope focal plane. Such effects, integrated in time, result in enlargement of the point-like sources images and a loss of the resolving power.

2.2   How to define the shape of the wavefront

Now we define the mathematical representation of the wavefront shape. We take advantage of a sequence of polynomials to describe the wavefront measured by the sensor. To do this we use the mathematical formulation of Frits Zernike (1934). He derived a sequence of orthogonal polynomials on a unitary circle, that allows to build any shape as combination of these (Wyant, 2008, [21]). Every polynomial draws up a specific shape on the unitary circle with amplitude provided by a coefficient that multiplies the polynomial. Finally every polynomial of the sequence with its coefficient is summed with the others to obtain the overall shape.

The advantages of this set of polynomials are:

1. they are orthogonal over the continuous unit circle. In particular, every polynomial is independent from the others and the variation of the weight of a polynomial does not affect the rest of them. Furthermore the set is continuous and its derivative is continuous;

2. the sequence of polynomials is obtained by a series that extends to infinite, so the number of polynomials is infinite. This fact allows to model an arbitrary complex shape;

3. we can break off the sequence to any polynomial. This reduces the complexity of the computation and the complexity of the shape. Furthermore it is possible to remove a specific polynomial from the set without influencing the others.

From the introduction of the first sequence of polynomials by Zernike, others mathematicians have developed more sequences of polynomials. These sequences differ from that of Zernike for the sequential order of the polynomials and for the specific normalization with which are defined. In this thesis we have chosen the sequence of polynomials Zernike ANSI (Thibos, 2000, [22]).

2.2.1   Zernike ANSI

Here we describe the math at the basis of Zernike ANSI. We start to define the unitary circle coordinates of radius ρ and angle θ (see Fig. 2.4). The sequence of functions that we want to derive must be orthogonal on the unitary circle, so:

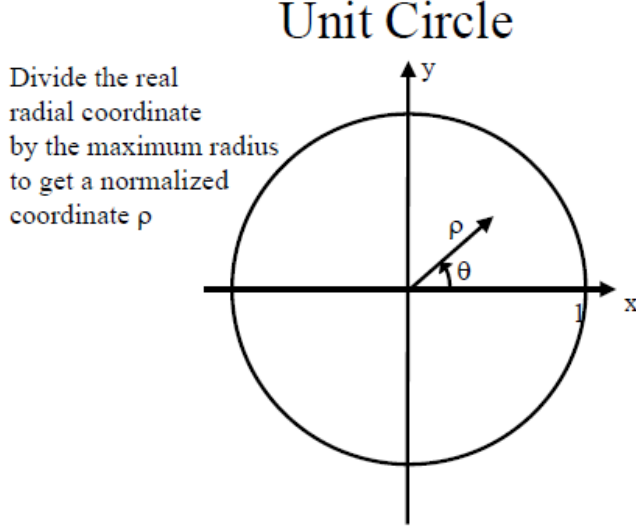$$\int_0^{2\pi} \int_0^1 V_i(\rho,\theta) V_j(\rho,\theta) \rho d\rho d\theta = C_j \qquad (2.12)$$

Unit Circle

Divide the real
radial coordinate
by the maximum radius
to get a normalized
coordinate ρ

Figure 2.4: Unit circle to define the orthogonal sequence of Zernike polynomials.

where C_j is a constant for a given j, if $i = j$, or it is 0 otherwise.

Then we separate the radial part from the angular part $V_i(\rho, \theta) = R_i(\rho)\Theta_i(\theta)$. Obviously the orthogonal propriety must remain:

$$\left[\int_0^1 R_i(\rho)R_j(\rho)\rho d\rho\right]\left[\int_0^{2\pi} \Theta_i(\theta)\Theta_j(\theta)d\theta\right] = C_j \qquad (2.13)$$

if $i = j$ or 0 otherwise. The sequence of polynomials Zernike ANSI is defined like this:

$$Z_n^m(\rho, \theta) = N_n^m R_n^{|m|}(\rho)\cos(m\theta) \text{ for } m \geq 0 \qquad (2.14)$$

$$Z_n^m(\rho, \theta) = -N_n^m R_n^{|m|}(\rho)\sin(m\theta) \text{ for } m < 0 \qquad (2.15)$$

where n is the radial order and m is the azimuthal order, while N_n^m is the normalization. The angular component is represented by sin() or cos(), while the radial component is defined as:

$$R_n^{|m|}(\rho) = \sum_{s=0}^{(n-|m|)/2} \frac{(-1)^s(n-s)!}{s![0.5(n+|m|)-s]![0.5(n-|m|)-s]!}\rho^{n-2s} \qquad (2.16)$$

From the normalization we obtain that $N_n^m = \sqrt{\frac{2n+2}{1+\delta_{m0}}}$ depends on n and m.

The first five polynomials are:

$$
\begin{align}
& \tag{2.17} \\
Z_0^0(\rho, \theta) &= 1 \tag{2.18} \\
Z_1^{-1}(\rho, \theta) &= \rho sin(\theta) \tag{2.19} \\
Z_1^1(\rho, \theta) &= \rho cos(\theta) \tag{2.20} \\
Z_2^{-2}(\rho, \theta) &= \sqrt{6}(\rho^2 sin(2\theta)) \tag{2.21} \\
Z_2^0(\rho, \theta) &= \sqrt{3}(2\rho^2 - 1) \tag{2.22} \\
Z_2^2(\rho, \theta) &= \sqrt{6}(\rho^2 cos(2\theta)) \tag{2.23} \\
& \tag{2.24}
\end{align}
$$

In the case where the images are matrices in xy coordinates (as in the experimental setup described in Chapter 4), the Zernike ANSI cartesian coordinates should be selected. In particular the center of the circle remains in the cartesian coordinates too, while $\rho = \sqrt{x^2 + y^2}$ and $\theta = \arctan(\frac{y}{x})$.

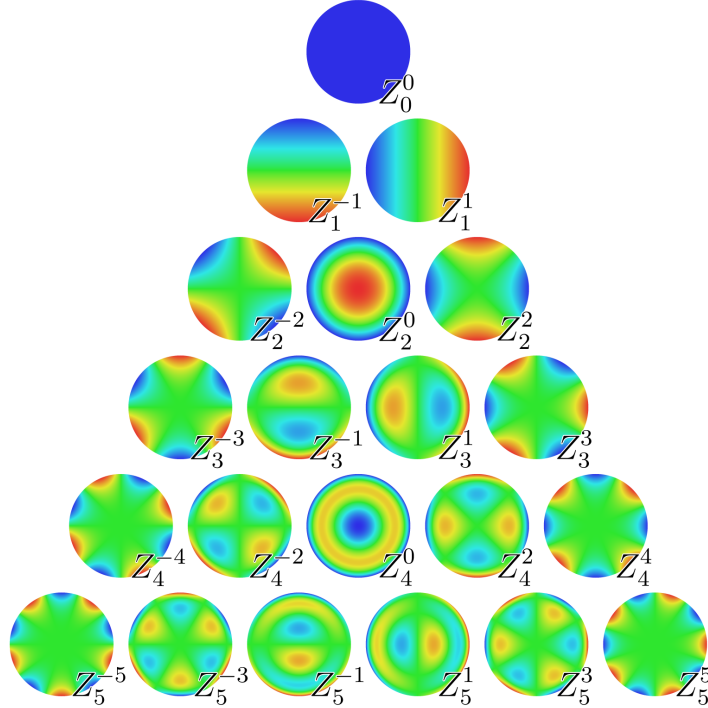The shape of the few first polynomials of Zernike ANSI are like to figure 2.5:

Figure 2.5: The shape of the first 21 Zernike polynomials, ordered vertically by radial degree and horizontally by azimuthal degree (Schwiegerling, 2002).

Chapter 3

Adaptive Optics system

This Chapter focus on the features of an Adaptive Optics system in general. It will dwell particularly on the wavefront sensor and on the deformable lens, the fundamental aspects of this thesis.

3.1 Components

After having defined the principal parameters of the atmospheric turbulence in Chapter 2, we can now describe an optical system that allows the measure of the deformations of the wavefront and successively its correction (Edwards, 2000, [23]). To be able to complete these operations, the AO system must be composed of three elements: the deformable optical element, the control system (computer) and the wavefront sensor.

3.1.1 Deformable optical element

The deformable element commonly used in AO is deformable mirror (DM). It can be composed of an array of flat micro-mirrors that form an single flat mirror or it can be composed of a single reflecting membrane (see Fig. 3.1). In the first case, each micro-mirror can move through actuators that allow different movements. A single actuator for micro-mirror produces only a translation, while more actuators for micro-mirror are able to tilt it. In the second case, the single reflecting membrane is deformed by the actuators set behind it (see Fig. 3.2). In general, the actuators can be of various types. Some actuators are composed of magnets that are moved by electric impulses, others are piezoelectric actuators that are able to change their static structure when electric charges flow inside it.
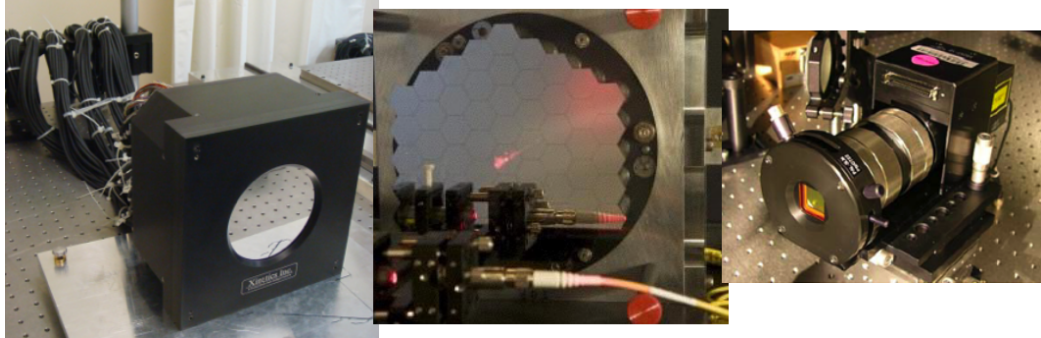
Figure 3.1: Example of deformable mirrors. From left to right: membrane DM, segmented DM and liquid crystal DM.
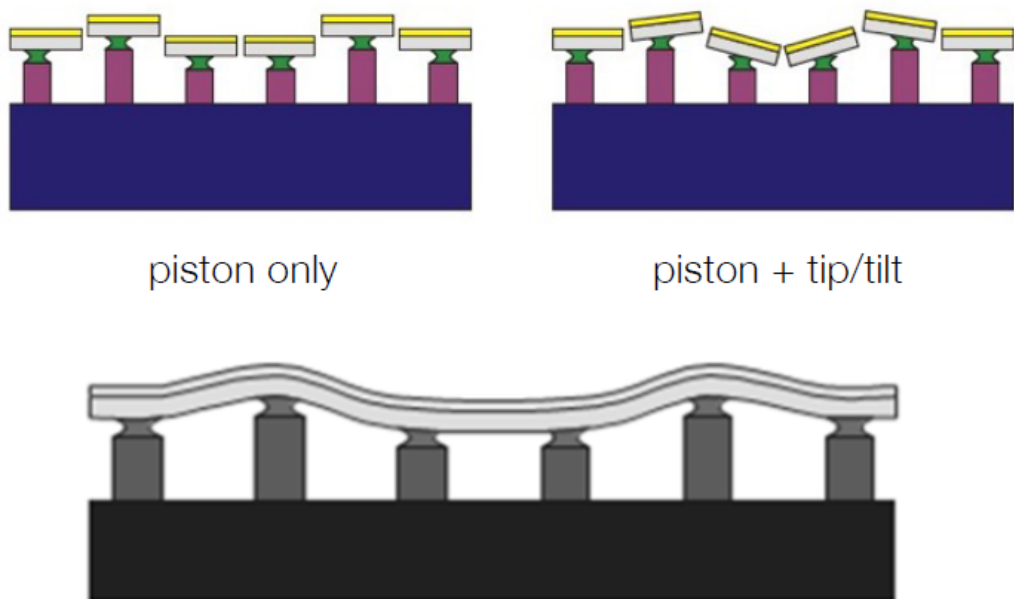

Figure 3.2: Example on working of micro-mirror DM (on the top) and membrane DM (on the bottom).

In this experiment, a new and innovative deformable optical element has used: the deformable lens designed at CNR-IFN of Padua in 2015 (Bonora, 2015, [2]). The DL is composed of two thin glass windows (thickness 150 *micron*), upon each of which is mounted a piezoelectric actuator ring (see Fig. 3.3). The gap between the windows is filled with a transparent liquid, mineral oil. The piezoelectric actuators have an external diameter of 25 *mm* and an internal diameter of 10 *mm* with a thickness of 200 *micron*. Both rings are divided into 9 sectors that can be actuated independently. The piezoelectric rings are glued to the windows and act as a bimorph actuator, such that the application of a voltage generates a deformation of the glass window. The actuators are controlled by a 18 channel high voltage ($\pm$ 125 V) driver. The 9 actuators on the top and bottom windows generate different effects because the top window is attached to the actuator by an elastomer foam that is free to move. To generate aberrations up to the 4th order it is necessary to have at least 15 actuators and a ring of actuators outside the active region. The bottom window is blocked at its edge by a rigid aluminum. This constraint moves the maximum (or the minimum) of the deformation inside the clear aperture (see Fig. 3.3(c-d)). Thus each actuator, although placed outside the clear aperture, acts as though it pushes the window from the inside. The shape of the top window can be restrained in the center by gluing a transparent disc of borosilicate glass (diameter $3mm$, $1mm$ thick, $n = 1.474$, see Fig. 3.3) with the same refractive index as the liquid. Deformation of the surfaces of the adaptive lens are illustrated in figure 3.3.

The current limit of the adaptive lens is the low number of aberration orders that it is able to correct. In fact, differently from the deformable mirror, the adaptive lens does not have any actuator across its diameter, but only near the edges. Therefore the radial orders, which the lens can form, are low: up to the fourth order of Zernike in this case. While there is no limitation on the azimuthal orders if the number of actuators increases. This features is the most important limitation of the deformable lens. While its capacity to form and to maintain a certain shape is equal to that of the deformable reflecting elements.

This deformable optical element is used specially in microscopy because it reduces the optical length of the system with respect to a common deformable mirror. In fact the classical deformable mirrors extend the optical path of the instrument due to the reflection, while the deformable lens can be inserted in a optical system without extending it. This is a desirable characteristic in microscopy, where the instrument must be as compact as possible. Nowadays it is possible to build a deformable lens with diameters of $5 - 25$ *mm* and with up to 18 actuators.
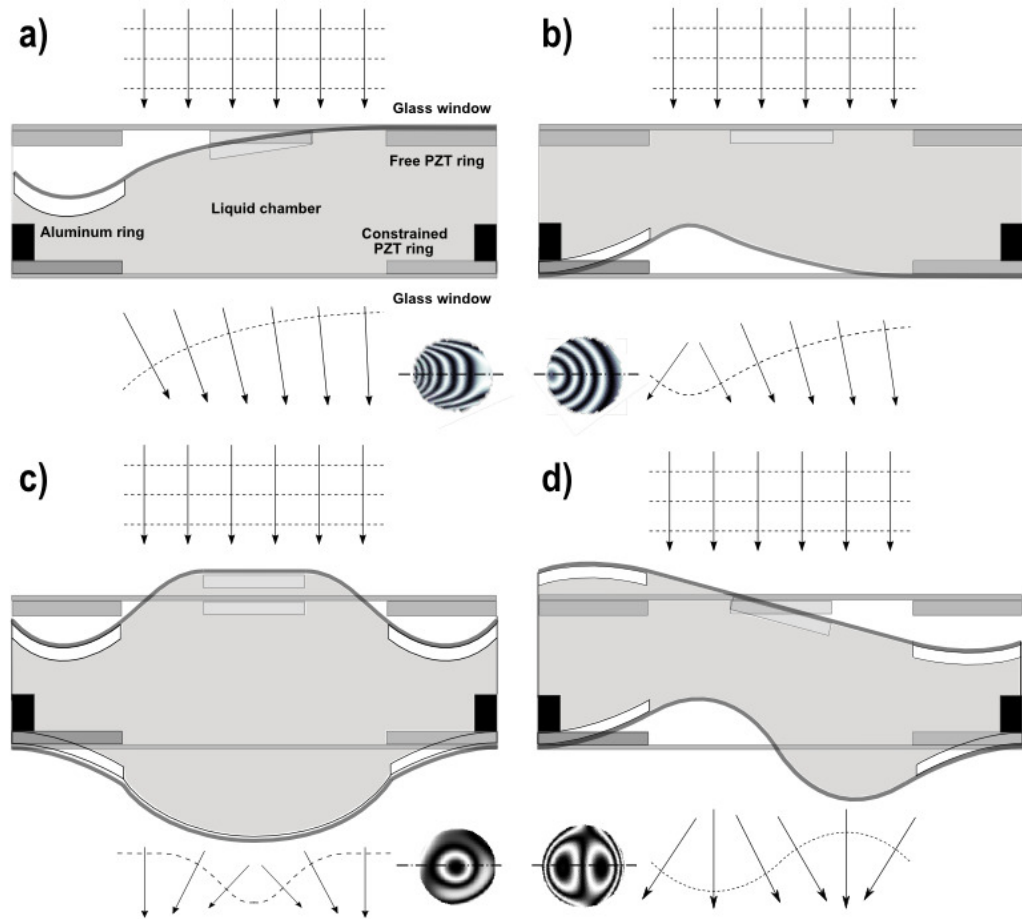
Figure 3.3: In this figure we can see how the deformable lens of Bonora et Al. works. In particular the figure shows the difference between the piston motion of actuator on the top membrane and the tilt motion of actuator on the bottom membrane due to constrain ring on the edge of piezoelectric ring (Bonora, 2015, [2]).

3.1.2 Wavefront control system

Concerning the control system, it must be able to receive the signals measured by the WFS, to reconstruct the shape of the wavefront and to compute the command vector of exit impulse to be sent to the deformable element to the correction of the wavefront. All these operations the control system has to do with a frequency greater than the Greenwood frequency (Chapter 2) and in stable way. Thus the reconstruction is applied to a wavefront with the same aberrations of that measured. Particularly the control system receives from the wavefront sensor the local gradient of the wavefront calculated on sub-aperture conjugated with the pupil of the telescope. Then the control system converts these gradients, that are the spatial derivatives of the wavefront, in a matrix of coefficients of some set of functions. In this case the functions are the Zernike polynomials. Finally, the control system computes the command vector, i.e. the vector that contains the voltages for each actuator to send to the deformable element to correct the aberrations, solving the equation $v = A \cdot \phi$ (Tyson, 2001, [1]). In this equation v is the command vector of the deformable element, ϕ is the phase vector of the wavefront and A is the command matrix that converts the aberrations measured in commands of deformable element. To solve this equation, the control system must know the command matrix A.

To obtain the command matrix, there are two approaches: zonal method and modal method. The first method derives, before, the influence matrix and then it converts this matrix in the command matrix using the singular value decomposition (SVD) operation. The influence matrix P is obtained from the equation $\phi = P \cdot v$ sending to deformable element an unitary voltage for each actuator at a time. Subsequently the system measures the vector ϕ of the aberrations caused by the action of the single actuator. The join of the ϕ vectors for each actuator produces the influence matrix P. The second method derives the influence matrix P activating the deformable element modes instead of single actuators. Here the zonal command vector v is replaced by the modal coefficients c. Typically, the deformable element modes are chosen to be the approximation of the Zernike modes or others mathematical modes (Korkiakoski, 2008, [24]). Similarly to the zonal method the command matrix A is obtained by the SVD operation of the influence matrix P measured. The difference between the two method is, substantially, the way with which the influence matrix is derived. In particular, the difference of the command vectors send to the deformable element to reconstruct the influence matrix.

In this case, the zonal method is been used to derive the command matrix of the deformable element. In fact, the deformable element have to be cali-

brated, in particular the matrix of influence, i.e. how the deformable element is deformed by every single actuator. The control system sends the impulse to the deformable element proportional to the command matrix multiplies by the aberration vector. In particular, the control system has to know the command matrix, i.e. the inverse of the influence matrix, that can be obtained with the SVD. To do this, we start from the equation:

$$
\begin{bmatrix} \phi_1 \\ \vdots \\ \phi_m \end{bmatrix} = \begin{bmatrix} p_{11} & \cdots & p_{1n} \\ \vdots & & \vdots \\ p_{m1} & \cdots & p_{mn} \end{bmatrix} \times \begin{bmatrix} v_1 \\ \vdots \\ v_n \end{bmatrix} \tag{3.1}
$$

where the ϕ vector is the phase of wavefront, the matrix P is the influence matrix and the v vector is the command vector. To find P in $\phi = P \cdot v$, we can set v equal to one and measured the resulting ϕ, i.e. we set one actuator at a time to one unit and the WFS measures the resulting phase. We repeat this measurement for each one of the n actuators.

$$
\begin{bmatrix} \phi_1 \\ \vdots \\ \phi_m \end{bmatrix} = \begin{bmatrix} p_{11} & \cdots & p_{1n} \\ \vdots & & \vdots \\ p_{m1} & \cdots & p_{mn} \end{bmatrix} \times \begin{bmatrix} 1 \\ \vdots \\ 0 \end{bmatrix} = \begin{bmatrix} p_{11} \\ \vdots \\ p_{m1} \end{bmatrix} \tag{3.2}
$$

In this way, the system reconstructs the total matrix P. So it obtains the command matrix A as inverse of P. In this work the vector of the Zernike coefficients will used instead of the phase vector.

3.2 Wavefront sensors

The wavefront sensors most used are: the Shack-Hartmann WFS and the pyramid WFS. In this thesis both the SH-WFS and the P-WFS are used. This Section explains their functioning in details and the various features that differentiate each other.

3.2.1 SH wavefront sensor

The Shack-Hartmann sensor is composed by an array of micro-lenses that is placed at the focal distance from the detector (see Fig. 3.4). In this way, positioning the array of micro-lenses on a pupil plane of an optical system, the pupil is divided in sub-apertures, one for each micro-lens of the array. The local gradient of wavefront is measured by considering the displacement of the spots on the sensor with respect to each optical axis of the micro-lenses.
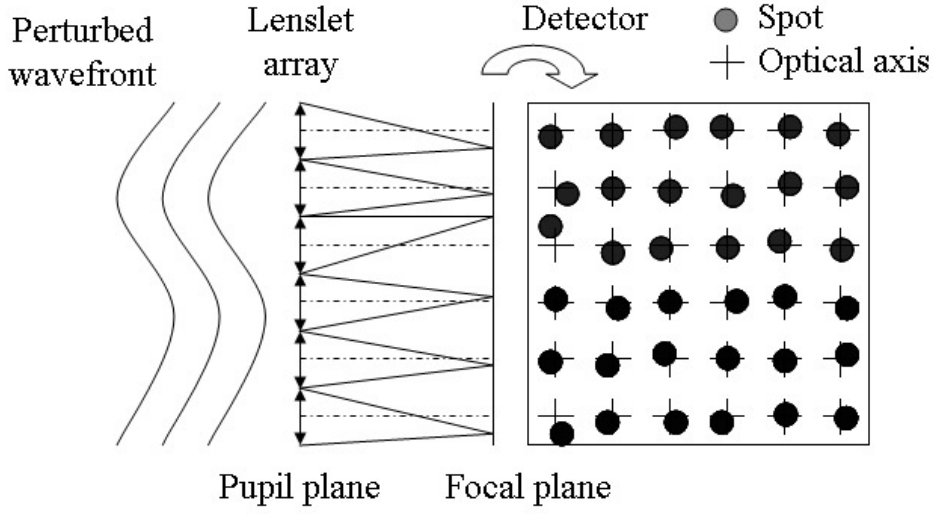
Figure 3.4: Example of Shack-Hartmann sensor. The perturbed wavefront is divided by the micro-lenses array and an equal number of spot are formed in the detector. The displacement of every spot with respect to its optical axis determines the local spatial derivative of the wavefront.

Particularly, if the wavefront coming from the astronomical source enters deformed on the pupil of the telescope, the deformation will be obtained as local tilt of every sub-aperture given by the dimension of the micro-lens projected on the pupil of the telescope. Therefore the smaller are the micro-lenses and the more sampled is the wavefront, but every sub-aperture collects less photons decreasing the signal-to-noise. The inclination of wavefront for each sub-aperture is proportional to shift of the spots on the sensor as follow:

$$S_x = \frac{\Delta x}{f_{array}} \tag{3.3}$$

$$S_y = \frac{\Delta y}{f_{array}} \tag{3.4}$$

where S_x and S_y are the local gradient of wavefront on sub-aperture in radians, Δx and Δy are the shifts of spots on the sensor in meters and f_{array} is the focal length in meters of the micro-lenses.

Another method to derive S_x and S_y is the Quad-Cell system. In this case we consider a portion of area of the CCD centering in the optical axis of the micro-lens. This area is divided by two orthogonal axis in four quadrants. Instead of measuring the displacement of the spot with respect to the optical axis, we measure the local gradient of the wavefront as the difference of

intensity between the four quadrants. In fact, the displacements of the spot
with respect to the optical axis brings a variation of intensity between the
four quadrants (see Fig. 3.5). In this way, if the spot is centered in the
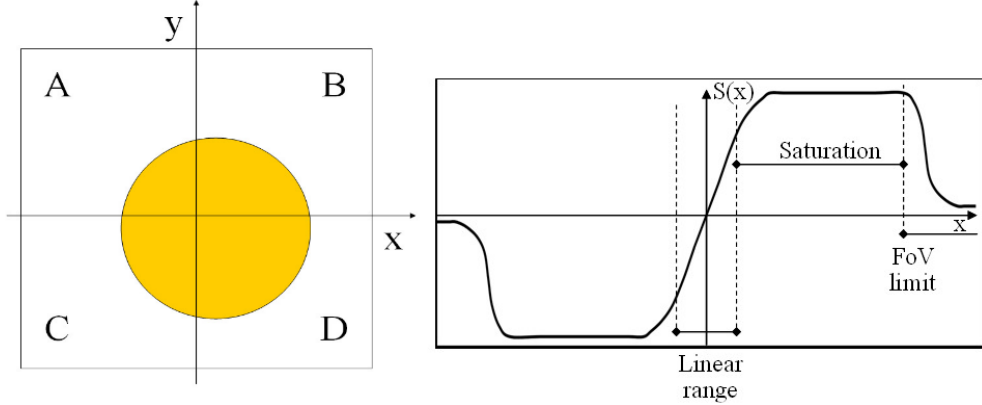

Figure 3.5: On left the Quad-Cell concept applied for each spot of the micro-
lenses array; on right the S_x signal as a function of the spot shift along the
x axis.

optical axis of the micro-lens, the four quadrants have the same intensity
and so the local wavefront is flat. In the other side, if the spot is shifted with
respect to the center of the optical axis of the micro-lens, the four quadrants
have different intensity and so the local wavefront is tilted. The Quad-Cell
equations for the first spatial derivative of the wavefront are:

$$S_x = \frac{B + D - A - C}{A + B + C + D} \tag{3.5}$$

$$S_y = \frac{A + B - C - D}{A + B + C + D} \tag{3.6}$$

where A, B, C and D are the four intensity for each quadrant. The principal
problem of this method is that two equations, to define the first derivative
of the wavefront, are linear only for small movement of the spot with respect
to the optical axis. Then, for large displacement of the spot, the Quad-Cell
equations are no-linear and the system fails to measure the local gradient of
the wavefront (see Fig. 3.5).

3.2.2 Pyramid wavefront sensor

The P-WFS was been introduced by Ragazzoni et Al. in the '90s, and its
principal component is a pyramid prism. The pyramid is located on the focal

plane of the optical system, so it divides the PSF in four divergent beams following the formula:

$$\beta = \alpha \cdot (n - 1) \tag{3.7}$$

where β is the divergent angle of the beams in radians, α is the vertex angle of the pyramid in radians and n is the refractive index of the glass (see Fig. 3.6). Subsequently the four beams are re-collimated from a lens of focal
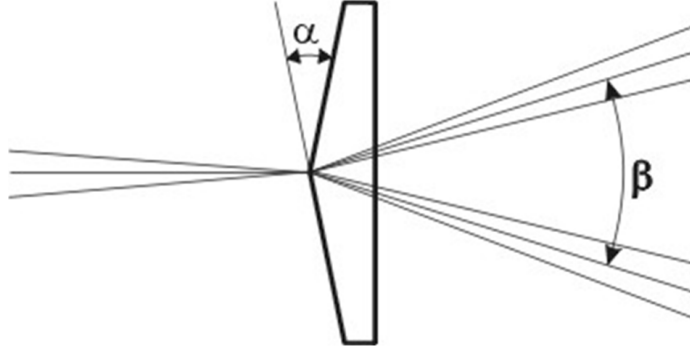

Figure 3.6: Scheme of the pyramid. We can notice β the outgoing angle and α the vertex angle of the pyramid.

F_{object}. After the collimator lens, a sensor (CCD) is set on the pupil plane. Therefore four images of the telescope pupil will be created on the sensor relative to a portion of PSF on each pyramid face. In this case the local tilt of the wavefront is measured on the pupil but the sub-apertures become the pixels of the sensor. In this way we can obtain the first spatial derivative of the wavefront from the difference of intensity among the corresponding pixels of the four images of the pupil (see Fig. 3.7):

$$S_x = \frac{B + D - A - C}{A + B + C + D} \tag{3.8}$$

$$S_y = \frac{A + B - C - D}{A + B + C + D} \tag{3.9}$$

where A, B, C and D are the intensities of the pixels in the same position with respect to the center of the four pupils. The signals S_x and S_y are proportional to the first spatial derivative along x and y of the wavefront. These two equations are namely the Quad-Cell equations. In fact, the Quad-Cell equation defines the local spatial derivative of the wavefront as previously described in SH-WFS. But, instead of computing the Quad-Cell for each sub-aperture, the P-WFS use the difference of intensity between the singular pixels; the singular pixel becomes the new sub-aperture in the P-WFS.
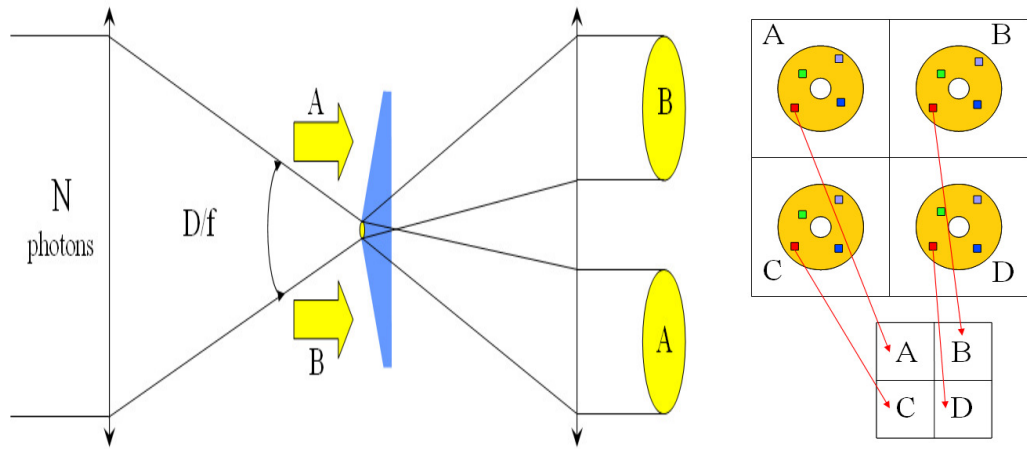
Figure 3.7: Scheme of the four pupil re-imaging in the pyramid WFS. The local spatial derivative of the wavefront can be compute as the different of intensity among the corresponding pixels of the four images of the pupil. The global Tip/Tilt can be computed as different of intensity between the overall pupils.
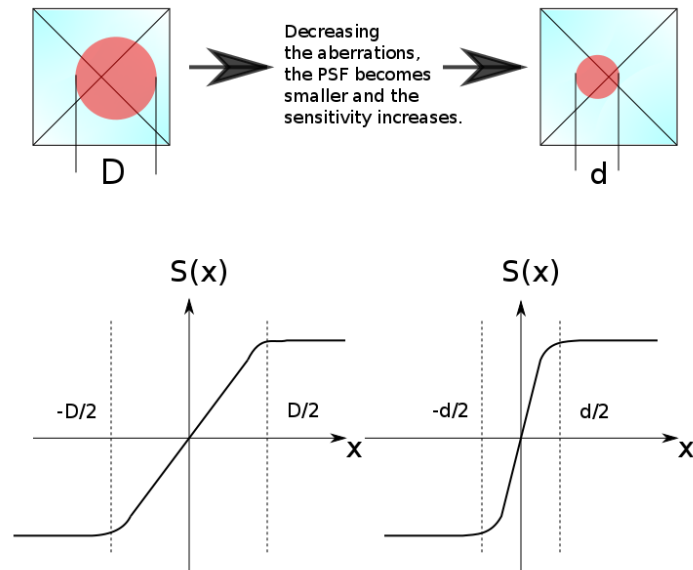

Figure 3.8: Scheme of the increasing of the P-WFS sensitivity with the decreasing of the wavefront aberrations. On top the variation of the PSF in the pyramid pin; on bottom the increasing of the P-WFS sensitivity due to increasing of the slope of linear range when the aberrations are eliminated.

From the previous equation we can deduce that the aberrations measured by the P-WFS do not depend on the intensity of the reference source. In fact, the aberrations are obtained as relative intensity between the four pupils, therefore, if the intensity of the source increases or the exposure time of the P-WFS camera increases, the values of the aberrations do not change. Instead, the sensitivity of the P-WFS changes with the mean intensity on the four pupils. In fact, if the intensity of a deformed wavefront increases, the aberrations remain constant, while the difference of intensity between the four pupils increases and the sensitivity too. Moreover the sensitivity of the P-WFS increases as much as the aberrations decreasing. The maximum sensitivity is reached when the PSF on the pyramid pin becomes diffraction limit (see Fig. 3.8). Therefore, when the aberrations of the wavefront are reduced, the P-WFS becomes more sensitive of small variations of the aberrations. In the other side, a bin of the pixels can enlarge the sub-apertures and so decreasing the Poisson error and the sensitivity too for the measurement of the fainter sources. Therefore the P-WFS is able to measure aberrations with fainter sources with respect to the SH-WFS. This is the most feature of the P-WFS.

3.3   Open or Closed loop

After describing all necessary components to Adaptive Optic, this Section exposes how these components cooperate in the system in order to correct the wavefront aberrations. Following the optical path of the light coming from the source, there are substantially two ways with which the optical circuit can correct the wavefront: open loop or closed loop (Le Due, 2002, [25]). These two ways are independent from the typology of components or wavefront sensors used.

In the first case, open loop, the light of a source captured by the telescope encounters as first element the wavefront sensor. Then the control system elaborates the data to send to the deformable element that corrects the aberration measured (see Fig. 3.9). This case is simpler to realize and also more stable from the computer point of view. In fact the control system has to calculate only the slopes and it reconstructs the wavefront from these. Then it sends the correction calculated to the deformable element to eliminate the aberrations of the wavefront.

The problems of this system are substantially two:

1. we do not have any information about the aberrations introduced by the deformable optical element, so we can not correct them;
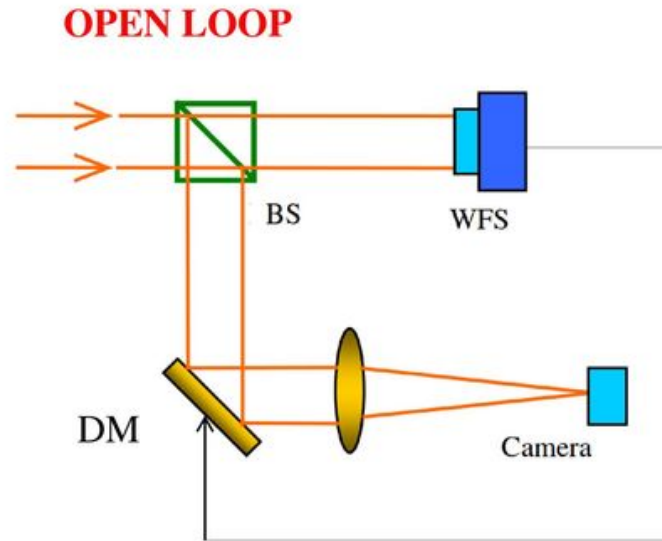
Figure 3.9: Example of open loop system. The wavefront reaches before the WFS and then the deformable element. The system does not get any information about the error of the correction.

2. we do not have any information about the shape of the wavefront after the correction. In fact the sensor, since it set before the deformable element, does not acquire any information with respect to the state of the wavefront after the correction. Therefore this system does not provide any type of error compensation on the process.

In the second method, closed loop, the light encounters before the deformable element and then the wavefront sensor (see Fig. 3.10). In this case, the WFS measures the sum of the aberrations of the incoming wavefront and of the deformable element too. In this way the WFS measures the error made to correct the aberrations and tries to minimize it. This is an important feature of the closed loop with respect to the open loop, in particular when we want to know the performance on the correction.

The problems of this system are two:

1. in closed loop the WFS measures the errors made during the correction and tries to minimize them in each loop. In this way, we can not have any information about the aberrations of the incoming wavefront;

2. the second problem concerns the stability of the control system. In particular, the control system tends to reduces repetitively the errors measured on the wavefront, but, if it is not efficient, it is not able to
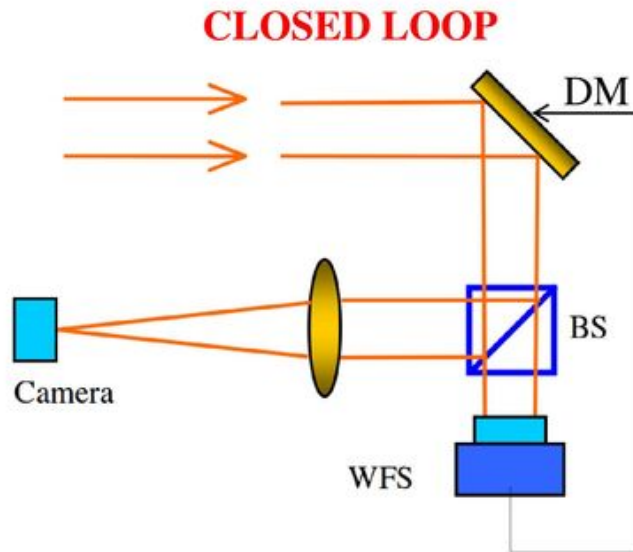
CLOSED LOOP

Figure 3.10: Example of closed loop system. The wavefront reaches before the deformable element and then the WFS. The system minimizes the error of the correction.

> eliminate all the aberrations also with infinite loops. This effect could bring to an instability in the control system.

The choice about the method to use depends on the nature of the measure that we want to get. Particularly, if we want to get information of the turbulence that creates the aberrations on the wavefront or we want the most stable control system, we must use an open loop. If the purpose is the elimination of the aberrations on the wavefront observed, it is preferable to use a closed loop. In fact, the closed loop allows to identify the errors on the correction and so to minimize them.

3.3.1   Discussion between P-WFS and SH-WFS

Now we enter in detail about the differences between P-WFS and SH-WFS, in particular the errors about the two system. The SH-WFS receives the total flux collected by the telescope aperture, since the pupil is not masked. The measured Tip/Tilt coefficients actually corresponds to the mean inclination of the wavefront in the selected sub-aperture. As many Quad-Cell WFSs as the total number of spots (corresponding to the micro-lenses number in the array) are positioned in the focal plane. If the wavefront is perfectly

flat and so its inclination is zero, each spot barycenter will be focused on the optical axis of the corresponding lens, but if, on the contrary, the wavefront is perturbed, the image focused by each lens will move on the focal plane, accordingly to the local gradient of the wavefront itself. The SH-WFS sensitivity is fixed and depends upon the spot radius, that is related to the micro-lens dimension according to the Airy equation. Obviously, since each spot is created by one micro-lens, its angular dimension will no longer be $\theta = \frac{\lambda}{D}$, with D the telescope diameter, but it will become $\theta_{SH} = \frac{\lambda}{d}$, where d is the dimension of the incoming wavefront area selected by a single micro-lens. If the number of sub-apertures is NxN, then $d = \frac{D}{N}$, so the spot angular dimension will increase to $\theta_{SH} = \frac{\lambda N}{D}$. To optimize the sampling, accordingly to the mean value of the Fried parameter of the astronomical site, $N \approx \frac{D}{r_0}$, and the spots are expected to move quite independently from each other (even if the low-order aberration effects, i.e. deformations on scales larger than r_0, will be similar for adjacent sub-apertures).

To quantify the Shack-Hartmann WFS error, we consider M the photons reaching the telescope entrance pupil in an integration time τ_0 (Greenwood frequency for frozen wavefront) and a micro-lenses array NxN. Therefore each sub-aperture collects about $n^* = M/N^2$ photons. The uncertainty to be associated to the measurement of the spot barycenter position depends on the number of incoming photons, in a perfect optical system, dominated by Poisson errors. Because of this uncertainty, which is intrinsic in the photon nature, the number of photons collected by the optical system is inside the range $M \pm \sqrt{M}$. This error propagates in the Quad-Cell signals expressions, resulting in:

$$S_x = \frac{\theta}{2} \cdot \frac{\frac{M}{2} \pm \sqrt{\frac{M}{2}} - (\frac{M}{2} \pm \sqrt{\frac{M}{2}})}{M \pm \sqrt{M}} \approx \pm \frac{\theta}{2} \cdot \frac{1}{\sqrt{M}} \qquad (3.10)$$

that results on an error of $\epsilon = \frac{spot-dimension}{2\sqrt{number-photons}}$. The uncertainty to be associated to the SH-WFS is then:

$$\epsilon_{SH} = \frac{\lambda}{D/N} \cdot \frac{1}{2\sqrt{n^*}} = \frac{\lambda}{r_0} \cdot \frac{1}{2\sqrt{n^*}} \qquad (3.11)$$

where $N = D/r_0$ is assumed as the number of sub-apertures across the diameter. If we consider a flat wavefront, only affected by Tip/Tilt aberration, all spots in the SH-WFS will move by the same amount in the same direction. The uncertainty on the signal will then be:

$$\epsilon_{SH_{tilt}} = \frac{\lambda}{Nr_0} \cdot \frac{1}{2\sqrt{n^*}} = \frac{\lambda}{D} \cdot \frac{1}{2\sqrt{n^*}} \qquad (3.12)$$

Summarizing, the SH-WFS can retrieve the wavefront aberration concerning both low and high orders, but it presents also some technical difficulties. The micro-lenses array is constituted by a lot of optical surfaces, that need to be produced with restricted specifications. In particular both the surface accuracy and the optical power must be homogeneous and accurate. Furthermore the most difficult is represented by the conjunctions between the lenses, since the wider is the gap, the higher the amount of light that is lost and diffused because of diffraction, also introducing noise on the CCD. Everything is made even more complicated by the fact that the alignment of such an array with respect to the detector is not straightforward.

In the P-WFS, a square-based refractive pyramid is positioned on the system focal plane at the location of the reference star image and it splits the light into four beams (namely the four areas of a Quad-Cell WFS), that are re-imaged by a lens into four pupil images on a detector. One of the Pyramid-WFS advantages is that, since the 4 pupils are re-imaged on a detector, the wavefront sub-apertures are defined at the level of the CCD. In particular, if four corresponding sub-apertures are defined onto the 4 pupil images (corresponding to the colored squares in figure 3.7), the local tilt can be retrieved in the selected sub-aperture, using the usual analytic expressions for S_x and S_y. It can be done because the light corresponding to the considered sub-aperture is divided into 4 parts by the pyramid. In such a way, the high order wavefront reconstruction can be performed. Another advantage of the pyramid WFS is given by the Poisson error, that is reduced with respect to a SH-WFS. In fact, the spot dimension on the pin of the pyramid in closed loop is λ/D, so the associated error will be:

$$\epsilon = \frac{\lambda}{D} \cdot \frac{1}{2\sqrt{M}} = \frac{\epsilon_{SH_{tilt}}}{N} \tag{3.13}$$

where λ is the working wavelength, D the telescope diameter, M the number of incoming photons, N the number of micro-lenses in the SH array, sampling a pupil diameter, and $\epsilon_{SH_{tilt}}$ the SH-WFS Poisson error.

Additional advantages are (Viotto, 2012, [20]):

1. the gain can be varied. When the AO system is activated, the deformable element is commanded by the RCT accordingly to the information retrieved by the WFS, up to the loop closing, when the spot size on the pin of the pyramid, starting from the seeing-limited value of $\theta_{seeing} = \lambda/r_0$, tends to its diffraction limit value of $\theta_{dl} = \lambda/D$. Because of this reason, the WFS sensitivity to the spot movements (i.e. the tilt, being it global or local) increases, allowing a wider dynamical range in the first AO iterations and a higher sensitivity when the loop

is closed. Moreover, when the loop is closed, the SNR increases considerably, consequently translating into an increasing of the theoretical limiting magnitude of the WFS;

2. since the spatial sampling is done at the level of the detector, it is easy to change the number of sub-apertures, accordingly to the seeing value. The real gain in this can be achieved when a detector allowing a direct rebin of the pixels before the charge reading is used, since it can considerably reduce the Read-Out Noise. In this case, a rebin matching the sub-apertures dimension can be chosen, to optimize the sampling accordingly to r_0, dividing the pupil image into D/r_0 sub-apertures and minimizing the RON;

3. the pyramid and the pupil re-imager are quite easy to be aligned to the CCD, if compared to a whole micro-lenses array.

On the other side the disadvantages are:

1. the first disadvantage of P-WFS is the low range of linearity. It can correctly works only with small aberrations. In fact, in the P-WFS there is a linear match between the shape of wavefront measured and the the set of coefficients of Zernike polynomials. However, this is true only in the linear range, therefore if the aberrations are small. If we have a strong aberration, the P-WFS saturates, i.e. it does not measure over some amplitude of the aberration. This problem affects the system at the start of the closed loop, but it can be overcome low-order;

2. the second problem is the calibration of wavefront sensor. In fact, as we will see in the next Chapter, the P-WFS feedback depends on the optical setup used and on the size of the PSF on the pyramid pin. Therefore, the calibration coefficient changes with the optical setup and with the strength of aberrations too;

3. the last disadvantage is the position of the pyramid's pin, that must be in the focal plane of telescopes in the same point of the PSF reference source in absence of aberrations. This can lead to some complications in the optomechanics setup, in particular with the alignment of the pyramid.

As regards the first and the third disadvantages, it is implemented in P-WFS a mechanic oscillation of the pyramid pin in the orthogonal plane with respect to the optical axis (see Fig. 3.11). This modulation of the pyramid brings to sample a wider area in focal plane. Therefore, if the control system
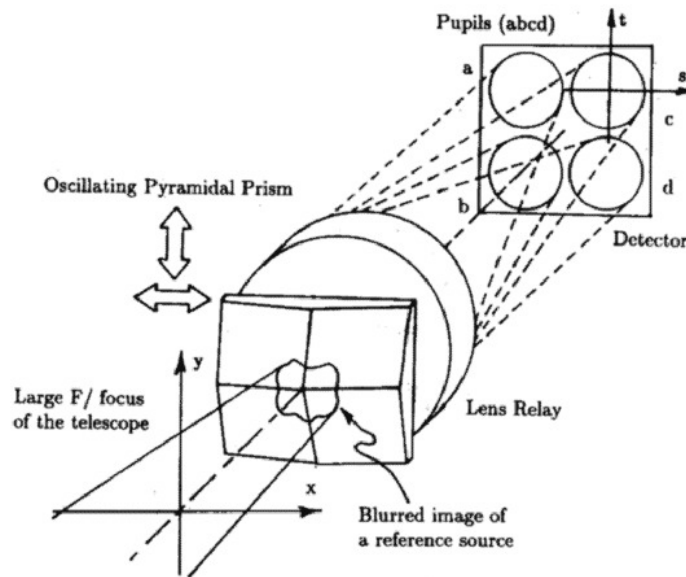
Figure 3.11: Example of P-WFS with the modulation on x-y axises. The P-WFS modulation is due to the oscillation of the pyramid on the x-y plane.

takes account of this movement, the modulation allows to expand the linear range of the sensor, but it reduces the sensitivity of the pyramid (Ragazzoni, 1996, [5]; Martin, 2015, [26]). Another method, which allows to expand the linear range of the pyramid sensor, is the diffusing plate. It permits to enlarge the PSF in the pyramid pin, but decreasing the sensitivity of the P-WFS (Ragazzoni, 2002, [6]). However these techniques will not use in my thesis.

Chapter 4

Experimental setup of the AO systems

The purpose of this thesis is the investigation of the sensitivity gain of the P-WFS when the NCPA are eliminated by a DL. In particular how the aberrations due to non common path involve into the wavefront correction and how much the P-WFS can gains in magnitude of the source with respect to the SH-WFS, if these aberrations are removed. To carry out this study, in the laboratories of the $IFN - CNR$ in Padua, an opto-mechanical setup has built with the aim to analyze the effects of non common path aberrations and to verify the usefulness of the DL in astronomy. The system is composed of two arms with two AO systems. The first arm is a closed loop with P-WFS. The second arm is a closed loop with SH-WFS, used to measure the non common path aberrations and it represents the "scientific" channel of the system. Furthermore a deformable lens is inserted in the optical path to correct the aberrations in closed loop with both WFSs (see Fig. 4.1). In microscopy, the deformable lens is used to compact the system and to correct the low-orders aberrations. In this thesis, instead, the DL is used to change and to eliminate non common path aberrations in the system. The idea is to correct the NCPA between the scientific channel (SH-WFS in this case) and the P-WFS by placing a DL after the beam splitter and before the pyramid. In this way, the DL acts only in the P-WFS arm and it does not influence the scientific arm. Therefore no bias are required to be introduced on the AO control and the pyramid can work at the maximum of its sensitivity without introducing any aberrations in the scientific arm. In this experiment, the DL has placed before of the beam splitter. In this way, we can measure the effects of the correction in both arms.
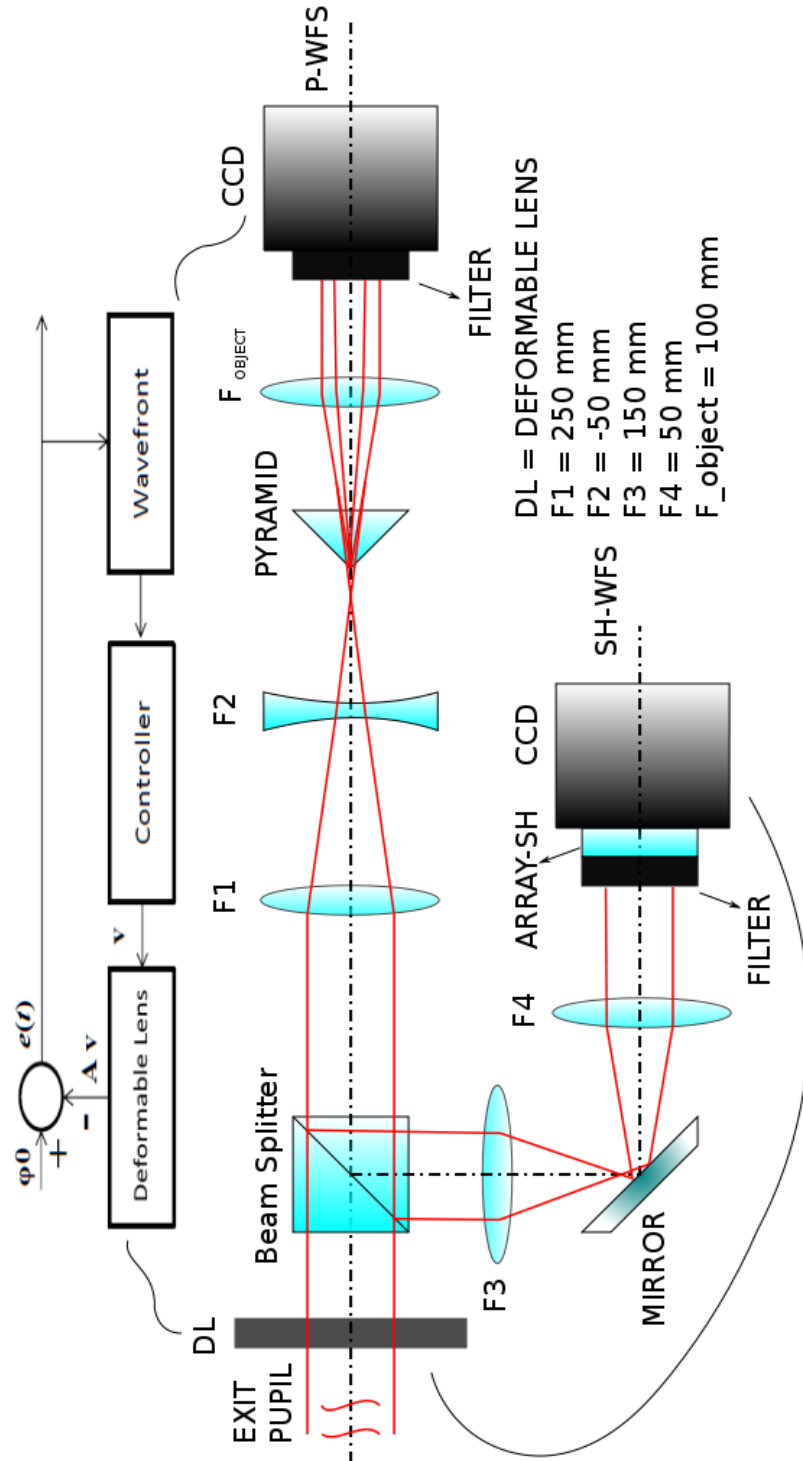
Figure 4.1: Scheme of the experimental setup composed of two arms: P-WFS arm in closed-loop and SH-WFS arm in closed loop.

4.1 Description of optical setup

Now this Section describes the optical setup of the P-WFS and the SH-WFS in the system. It explains, step by step, how components of the system has chosen and how they have been assembled in the laboratory. Then it describes the computer implementation and the calibration of the P-WFS.

4.1.1 P-WFS arm opto-mechanical setup

At the beginning, we implement a pyramid wavefront sensor that is able to correct the aberrations of wavefront in closed loop with a dedicated control system. During the thesis period, two pyramids were available. These pyramids have two different divergent angles β: the first pyramid has 0.5°, the second has 1°. To compact the system as much as possible, we choose the second pyramid, that splits the PSF of the source in four beams with a divergent angle greater than the first pyramid (see Chapter 2).

Figure 4.2: Images of the two pyramids: on the left the pyramid with divergent angle of 1°; on right the pyramid with divergent angle of 0.5°. The vertex angles are so small that we can not notice in the images.

In the first step, we compute the focal length of the collimator (F_{object}) that, after the pyramid, collimates the four divergent beams and it creates four images of the pupil on the camera (CCD). The distance between the centers of the four pupils along the diagonal follows $d_{center} = \beta \cdot F_{object}$. Therefore the longer is F_{object}, the more separated are the four pupils. Knowing that F_{number} must be a constant of the system, we calculate the minimum F_{number} for which the system separate the four pupils in the CCD without overlapping them, $F_{number_{min}} = F_{object} \cdot \sqrt{2}/d_{center}$ (see Fig. 4.3). The four pupils must be separated enough to cut out them with a squared mask, so the system has F_{number} greater than $F_{number_{min}}$. We choose a re-imaging lens, positioned after the pyramid in the optical path, with $F_{object} = 100\ mm$, then we obtain
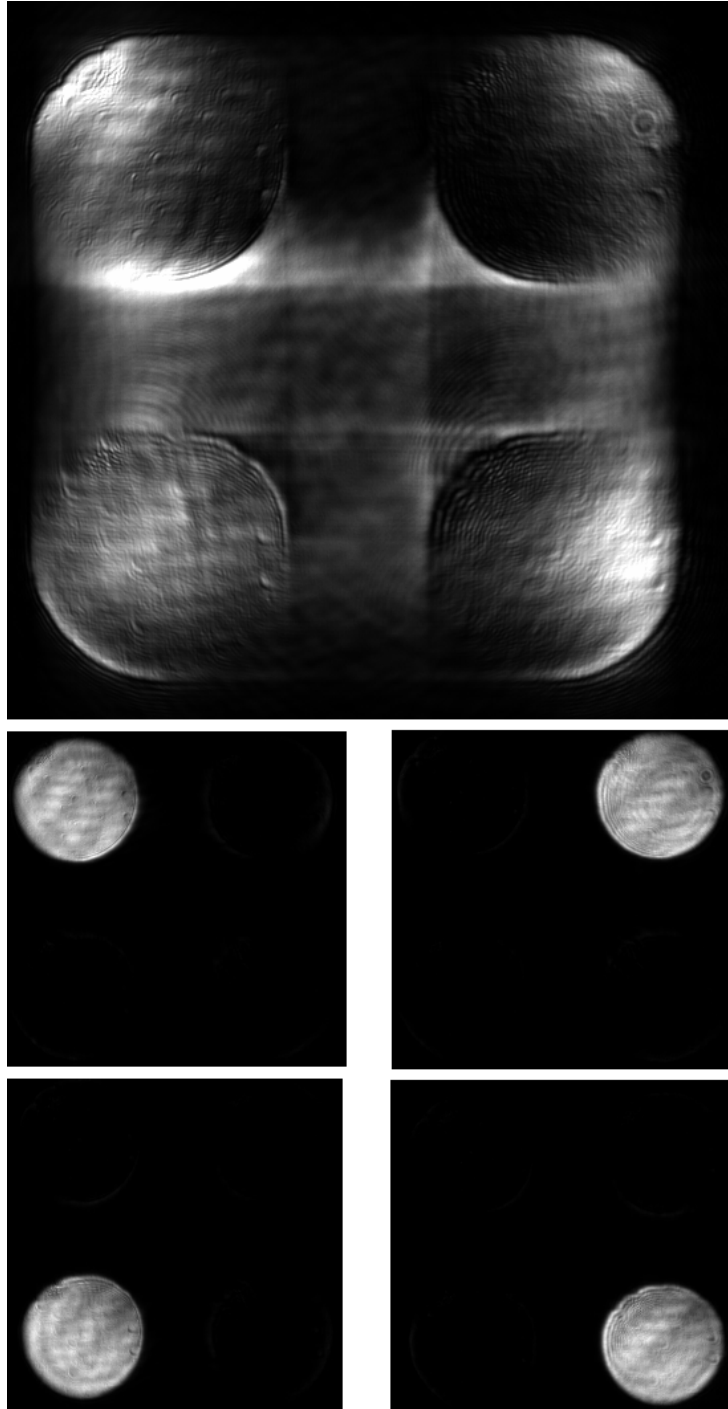
Figure 4.3: On top the image of the four pupils that the P-WFS takes to calculate the wavefront; the four pupils are not uniformly illuminated because of the aberrations. On bottom the four images of the four pupils take singularly.

$d_{center} \approx 1 \ mm$ and $F_{number_{min}} \approx 100$. A CCD is placed after the collimator lens in a plane conjugate with the pupil of the system. The CCD chosen has a pixel size of 5.2 *micron* and a resolution of $1280x1024$ pixel. In front of this CCD is placed a $NGG11$ filter with transmission of 1% to reduce the intensity of the incoming laser beam.

The deformable lens has a diameter of 10 mm and 18 actuators and it is used as pupil of the system. Therefore, to preserve the F_{number}, the lens before the pyramid must be a focal length longer than one meter. To compact the system we use a couple of lenses to build a Barlow's system. This system is composed of a positive lens with focal length of $F_1 = 250 \ mm$ and a negative lens with focal length of $F_2 = -50 \ mm$. Using these two sequentially and separating them about 210 mm, we obtain an equivalent lens with focal length greater than one meter, even if the length of Barlow system is about 400 mm (see Fig. 4.4).
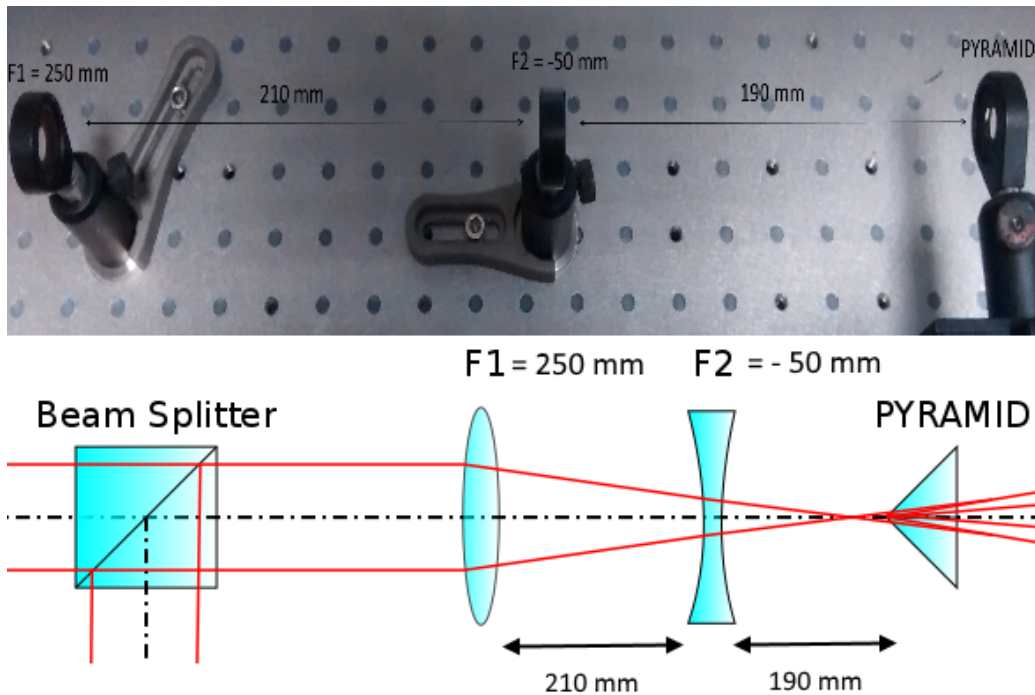

Figure 4.4: On top the image of the Barlow's lenses to increase the focal length of the system; On bottom the scheme of the Barlow's system.

This optical system composed of three lenses and a pyramid is aligned using a laser beam as reference of optical axis. The faces of the lenses are aligned with the optical axis using the back reflection of the laser beam at the surfaces of the lenses. The pyramid is installed on a translator xyz, where z

is along the optical path axis, y is the vertical axis and x is the horizontal axis (see Fig. 4.5). In this way we can move the pyramid to calibrate the
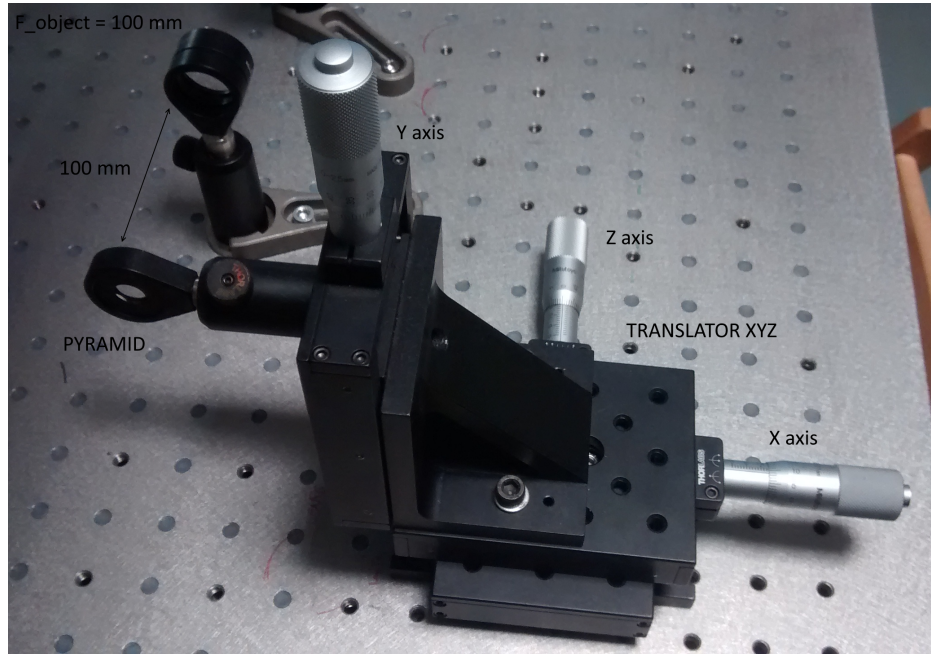

Figure 4.5: The image of the translator xyz where is attached the pyramid.

P-WFS and put the pin of the pyramid exactly on the PSF of the source. Finally, we insert the deformable lens on the conjugate plane with the CCD between the collimated laser source and the first lens F_1. Now the optical setup of the P-WFS is completed and it is composed as in figure 4.6.
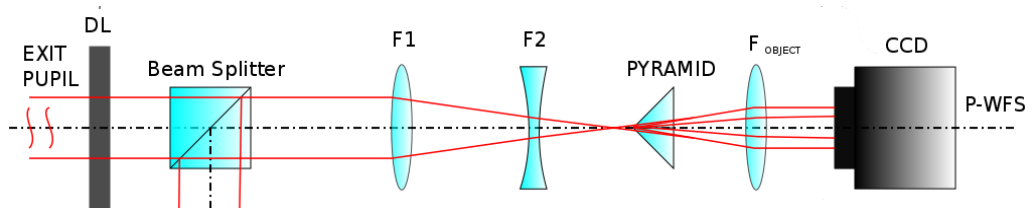

Figure 4.6: Scheme of the P-WFS in closed loop. From the left to right: the DL (the pupil of the system), the beam splitter for the scientific arm, the Barlow's system composed of F_1 and F_2, the translator with the pyramid, the collimator lens F_{object} and finally the CCD conjugate with the DL.

4.1.2 Control system implementation

The control system has the task to take images from the wavefront sensor, to elaborate these images, to extract the shape of wavefront and to send the commands to the deformable lens. All these operations spend time of computation. The control system must be efficient to save time, but also it must be accurate in the various steps. In this thesis, the control system is been implemented in *Matlab*.

The script (control system) implemented in *Matlab* can be split in three components. The first two are computed only at the beginning. They are related to the information about the position and the size of the pupils in the images and about the determination of the influence matrix to command the deformable lens. The third part of the script computes the aberrations measured during every loop.

The first part of the script is used to take four images of the four pupils singularly (see Fig. 4.3). To do this, we shift the pyramid with the translator to have the PSF on only one face at a time. From these four images the script derives the position of the center and the diameter for each pupil in pixel. In this case the mean diameter of the pupils is 170 pixels. But it is reduced of 10 pixels to eliminate the irregularity of the DL in the edge of it. Then the script uses a circular mask composed of a boolean matrix, where it is 1 inside the circle with size the selected diameter (160 pixels in this case) and 0 outside. Every pupil is cut out from the image and it is multiplied by the mask with the coincident position of the centers. This method is used to obtain four pupils with the same size. The script saves the centers and the selected diameter of the pupils, which can be used other times, if the optical system remains the same. After this step the script is able to fit the shape of a wavefront using a set of Zernike coefficients that represent the aberrations of wavefront itself.

The second part of the script deals with the calibration of the deformable lens, i.e. it extracts the influence functions matrix. The script, through a specific electronics, sends the signal to move one actuator at a time with constant voltage. Then the script takes an image with the actuator switched on and another with the actuator switched off. The first image contains the information about wavefront deformation due to the actuator plus the initial condition. The second image contains the information about the wavefront at the initial condition. The script computes the coefficients of Zernike and the shape of wavefront for the two images. Finally it obtains the vector column for this specific actuator as difference between the two sets of Zenike coefficients (see Section 3.1.2)(Korkiakoski, 2008, [24]). Once the script gets every vector column of influence for every actuator, the matrix of influence
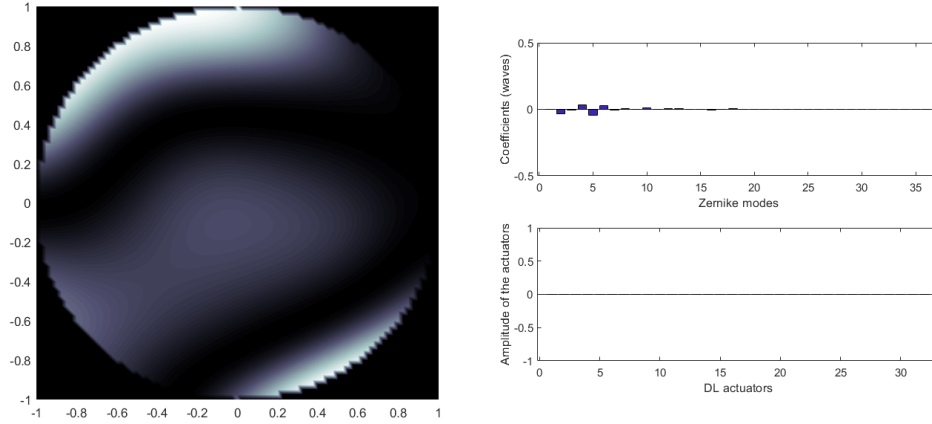
Figure 4.7: An example of the output script: on the left the interference pattern of the wavefront shape measured; on the right the values of the Zernike coefficients measured in waves (on top) and the values of the actuators that are set to zeros in this case (on bottom).

results to be the matrix composed of all influence vectors (Dalimier, 2005, [27]). The influence matrix, therefore, contains the information about the shape of the DL when the actuators are activated. Then the script calculates the inverse matrix using the SVD. Moreover, from the SVD, we get the singular values of the modes of the influence matrix. These values contain the information about how much strength the actuators require to reconstruct any mode of the Zernike ANSI (Dalimier and Dainty, 2005, [27]). The greater is the single value, the lesser is the strength required by the DL to reconstruct this mode. We remove the modes after the $10th$ from this matrix before to compute the inverse. In this way the script does not spend too much power on the actuators to restore the higher orders of Zernike. Then, making the inverse, we obtain the command matrix that it will be used to derive the command vector to send to the DL. Finally the script saves this matrix so that it can reads the matrix at the beginning of the operations.

The last part of the script is the process to correct the aberrations of the wavefront. The script takes an image of the four pupils and, after it has applied the mask, it computes the first spatial derivatives of the wavefront as in equation of the Quad-Cell (see Chapter 3). In this case the Quad-Cell is composed of the four pixels in the same position with respect to the centers of pupils. The script obtains two matrices: the matrix of the derivatives relative to the axis x and the other of the derivatives relative to the axis y. Then it fits these matrices with the matrices of the first spatial derivatives of the Zernike

polynomials (Noll, 1976, [28]; Mochi, 2015, [29]; Ramos-Lopez, 2016, [30]; Akondi, 2016, [31]). In this way it extracts, from the best fit, the set of Zernike coefficients and the shape of wavefront. This set of coefficients, which represents the aberrations of the wavefront, is multiplied by the command matrix to obtain the set of actuators signal to send to deformable lens.

In closed loop case, the script computes the residual aberrations and the commands to correct them, that are added to those of the previous measurement. This method is implemented with an integrator that has the following equation:

$$v(t) = v(t - T) + A \cdot c(t) \tag{4.1}$$

where $v(t)$ is the command vector to send to the deformable element, $v(t-T)$ is the command vector at the previous step, A is the command matrix and $c(t)$ is the Zernike coefficients vector measured in this step. In an ideal case, the script needs only one loop to correct all aberrations with this integrator. In reality, the integrator such formulated is unstable. In fact defining the math model as $c(t) = P \cdot v(t)$ and the error as $e(t) = c_0 - c(t)$, we can derive the following solution:

$$c(t + T) = P \cdot v(t + T) = \tag{4.2}$$
$$= P[v(t) + K \cdot e(t)] = \tag{4.3}$$
$$= c(t) + PK[c_0 - c(t)] = \tag{4.4}$$
$$= (1 - PK)c(t) + (PK)c_0 \tag{4.5}$$

the solution becomes:

$$c(t) = c_0 + (1 - PK)^{t/T}c(0) \tag{4.6}$$

this equation is stable, i.e. $c(t) \rightarrow c_0$ only when $| 1 - PK | < 1$. If we set $K = 1/P$ then $c(t)$ goes to c_0 in one time step T regardless of the value of $c(0)$. Therefore the control law is insensitive to small variations in process gain. Also it can be shown integral feedback is insensitive to small non-linearities and distortions. In reality the system sometimes is tending to oscillate or to be unstable, so a scalar gain G is inserted in the integrator:

$$v(t) = v(v - T) + G \cdot A \cdot c(t) \tag{4.7}$$

where G is the gain of the correction. From the previous demonstration, the gain G must be less than one if we want an integrator stable. In fact, as we can see in figure 4.8, if the gain G is set to a value equal or greater than one, the reconstruct becomes unstable and the RMS presents some peaks of instability during the closed loop. If the system would measure some dynamic
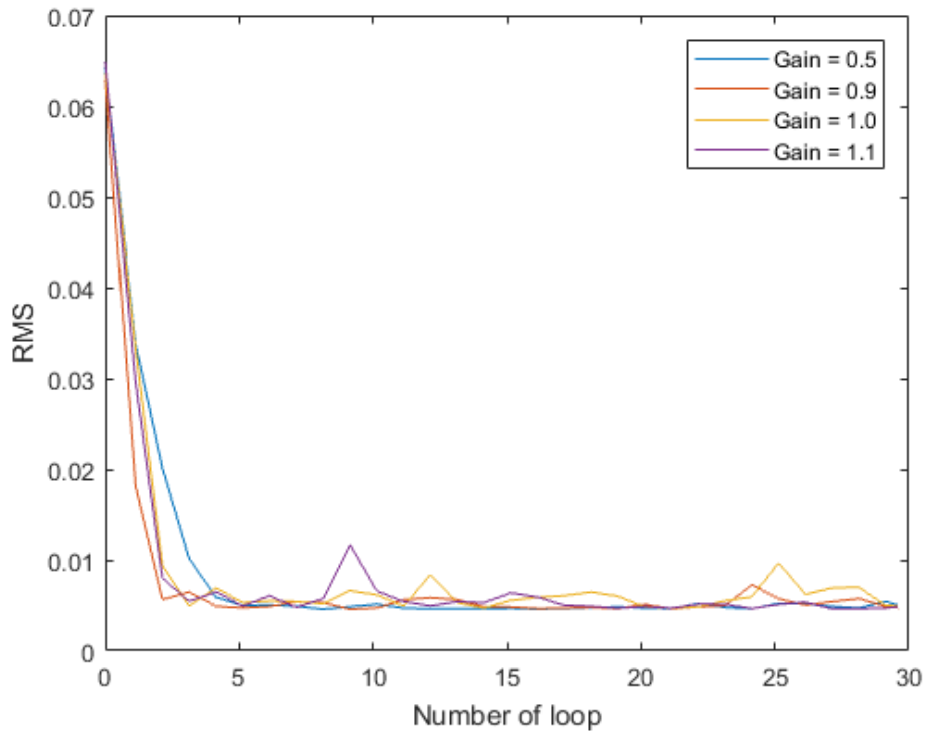
Figure 4.8: Plot of the P-WFS stability in closed loop varying the gain G of the integrator. In y axis the residual RMS in waves and in x axis the number of the loops. In this case we can observe some peaks of instability for the gain equal to 1.0 and 1.1.

turbulence, the instability increases and the peaks too. Setting the gain less than one, the closed loop needs more than a step to eliminate the aberrations. In particular, larger is the gain, lower is the number of loop used to correct the wavefront, but it becomes stable. In this case, the P-WFS can correct the aberrations in closed loop with a residual wavefront RMS of 0.005 waves (see Fig. 4.8).

4.1.3 Calibration of P-WFS

The first operation to be performed on the P-WFS system is its calibration. Namely we need to know the coefficients to convert the aberrations measured in unit of the system to metric unit or in waves unit. In fact, the aberrations are derived by the P-WFS as the difference of the intensity between the four pupils, but the Zernike coefficients such obtained are in unit of the system. However this conversion is only an indicative value of the system. In fact, as said in Chapter 3, the sensitivity of the P-WFS changes with the strength of the aberrations and the slope of the linear range too. Therefore the calibration coefficient depends on the Strehl ratio (SR) of the PSF on the pyramid pin and it is not a constant of the system. In particular, the SR is the ratio between the PSF of the deformed wavefront and the PSF in diffraction limit. Furthermore the calibration coefficient is not the same for every Zernike mode, but it depends on the radial Zernike order.

The conversion coefficient can be derived, for instance, shifting the pyramid along an axis of a known amount and evaluating the aberration induced on the wavefront. In particular, we take an image of the four pupils and subsequently we shift the pyramid along an axis with the translator. In this way, we induce an aberration of Tip/Tilt, if we shift the pyramid in xy plane, or we produce Defocus aberration, if we shift the pyramid along the optical axis. Therefore, we obtain three sets of Zernike coefficients, that are computed by the script from the images. In theory every set have only a coefficient of Zernike that changes, while the others remain constant. We plot these coefficients of Zernike against the displacement in metric unit (see Fig. 4.9 and 4.10). We obtain the saturation curve where the central zone is linear, while out of this zone the P-WFS tends to saturate, it is not linear, up to the value that does not change anymore.

The problem that arises in this procedure is the alignment between the xyz translator of the pyramid and the xyz axes of the optical path (this matching is very challenging to do). In fact, if there is a mismatching between the translator axes and the pyramid axes, there is variation not only for the coefficient of aberration along the axis shifted, but there is a small variation of the coefficient along the orthogonal axis too (see figures 4.9 and 4.10).
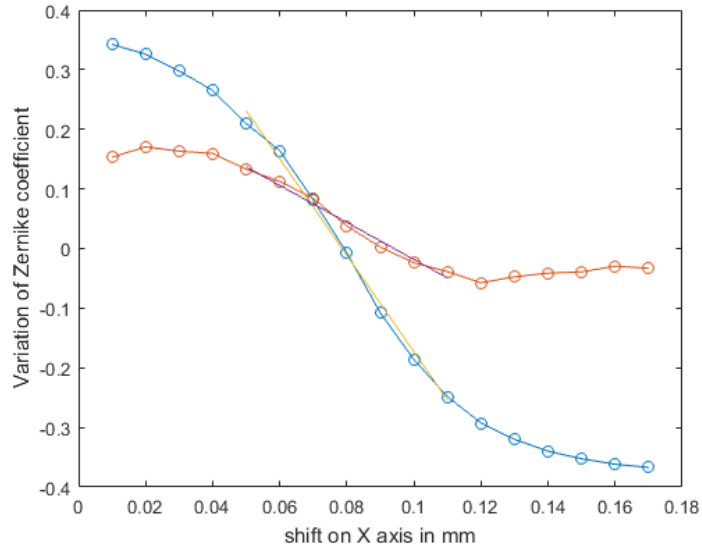
Figure 4.9: Plot of variation of Zernike coefficients in waves against the shift along the x axis. In particular in blue the Tilt X (3rd Zernike coefficient of the figure 2.5), while in red the Tilt Y (2nd Zernike coefficient of the figure 2.5). In yellow and purple the relative fitting lines of the linear portion.
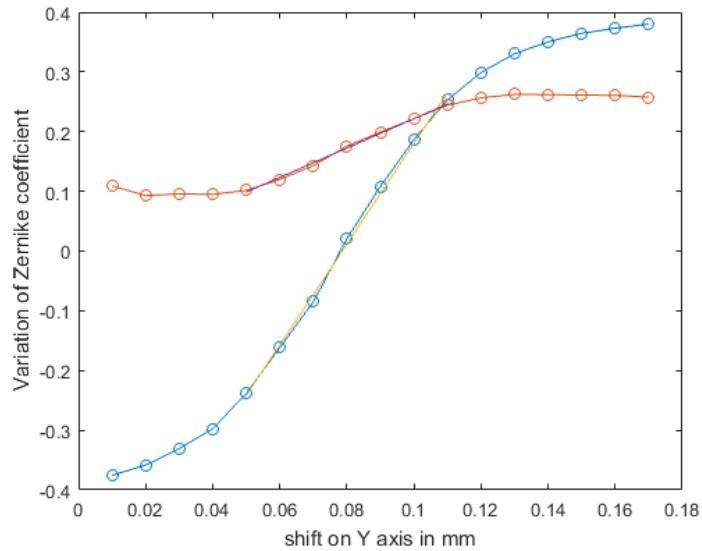

Figure 4.10: Plot of variation of Zernike coefficients in waves against the shift along the y axis. In particular in blue the Tilt Y (2nd Zernike coefficient of the figure 2.5), while in red the Tilt X (3rd Zernike coefficient of the figure 2.5). In yellow and purple the relative fitting lines of the linear portion.

This issue is solved returning the coefficients measured due to the shifting on the translator axis, into the theoretical coefficients due to the shifting on the optical path axis. To do this, we use the two angular coefficients of the lines, that fits the linear portion of the Tilt in x and in y, to derive the single one coefficients due to the shifting along the system axis. We compute this operation using the proprieties of the directional derivative.

Concerning the Defocus coefficient, the z axis of the translator is not perfectly aligned with the optical axis. Therefore, when we move the translator along the optical axis, there are small shifts on the orthogonal plane that lead to increase the Tip/Tilt coefficients of the system up to the saturation pattern. Moreover, the linear range of Defocus coefficient is very large, i.e. the this system on pyramid sensor has up to 20 mm of shifting on the optical axis without saturate. These two features lead to plot only the linear range of the Defocus coefficient. Furthermore the fit of the linear portion of the line is less precise due to arise of Tip/Tilt aberrations during the movements (see Fig. 4.11).
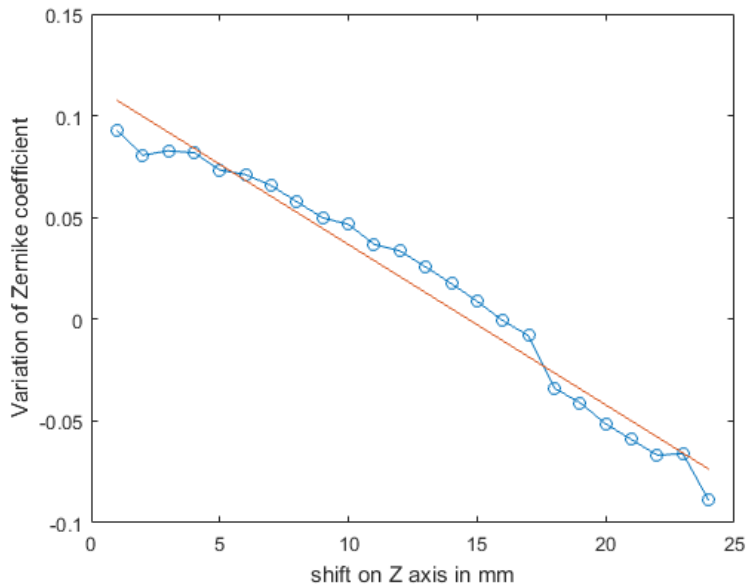

Figure 4.11: Plot of variation of Defocus Zernike coefficient in waves against the shift along the Z axis. The no-perfect linearity is due to the mismatching between the optical axis and the z axis of the translator.

The coefficients of conversion, between the specific unit of the system and the unit in meter, are obtained from the following equations:

$$conv_{defocus} = \frac{1}{2\sqrt{3}}\frac{1}{8} \cdot \left(\frac{1}{F_{number}}\right)^2 \cdot \frac{1}{m_{defocus}} \tag{4.8}$$

$$conv_{tilt} = \frac{1}{4}\frac{1}{F_{number}} \cdot \frac{1}{m_{tilt}} \tag{4.9}$$

$$conv_{tip} = \frac{1}{4}\frac{1}{F_{number}} \cdot \frac{1}{m_{tip}} \tag{4.10}$$

where $m_{defocus}$, m_{tilt} and m_{tip} are the angular coefficients of the lines that fit the linear portion of the curves. The fits have calculated the angular coefficients with confidence bounds of 95%. The three values of conversion are equal to $0.3 \cdot 10^{-6} \ \Delta c/\Delta m$, with c the Zernike coefficient. This value is been divided by reference wavelength ($630 \ nm$) to obtain the Zernike coefficients in waves unit.

Equations of calibration

This Sub-Section explains how to derive the last three equations for the calibration (Wyant, 1992, [32]). We start with Defocus calibration $conv_{defocus}$. We consider a convergent deformed wavefront and the other spherical wavefront relative to the first. This last wavefront is focused on point Q', while the first WF is focused on point O' as in figure 4.12. We call $R' - R = \Delta z$ the
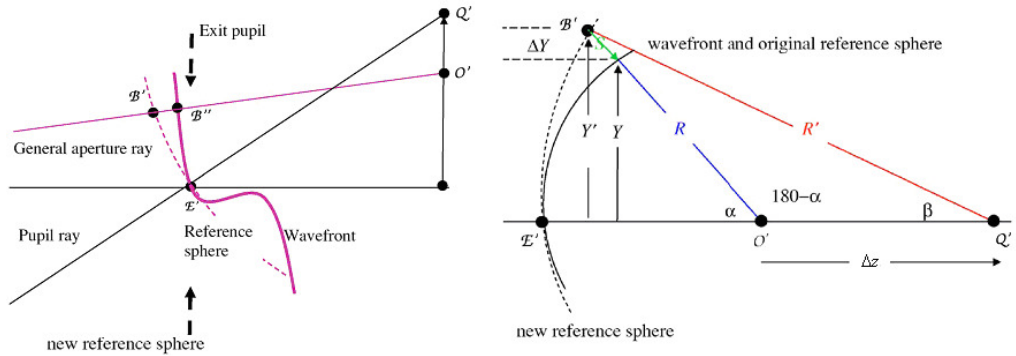

Figure 4.12: Scheme of the convergent deformed wavefront and the spherical wavefront relative to the first (on the left). Geometric scheme to calculate the segment S that represents the variation between the deformed wavefront and the ideal spherical wavefront (on the right).

distance between the two points along the z axis. If we consider the triangle $O\beta'O'_b$, we can define the segment $\beta'O'$ using the Carnot theorem:

$$(R^2 + S^2) = R'^2 + \Delta z^2 - 2R'\Delta z \cos\beta \tag{4.11}$$

from which we obtain:

$$S = \sqrt{R'^2 + \Delta z^2 - 2R'\Delta z \cos\beta} - R \tag{4.12}$$

To the Pythagoras theorem we know:

$$R'^2 - R'^2 \cos\beta = Y'^2 \tag{4.13}$$

from which we extract $\cos\beta$ using the Maclaurin series:

$$\cos\beta = \sqrt{1 - \frac{Y'^2}{R'^2}} \approx 1 - \frac{1}{2}\left(\frac{Y'^2}{R'^2}\right) - \frac{1}{8}\left(\frac{Y'^4}{R'^4}\right) \tag{4.14}$$

that we replace in the previous equation to obtain the following:

$$S = \sqrt{R'^2 + \Delta z^2 - 2R'\Delta z \left[\frac{1}{2}\left(\frac{Y'^2}{R'^2}\right) - \frac{1}{8}\left(\frac{Y'^4}{R'^4}\right)\right]} - R \tag{4.15}$$

since S is negligible and $R' \approx R$ if cos tends to one, then:

$$S = R\sqrt{1 + \frac{R'}{R^2}\Delta z \left[\left(\frac{Y'^2}{R'^2}\right) - \frac{1}{4}\left(\frac{Y'^4}{R'^4}\right)\right]} - R \tag{4.16}$$

Now we can also expand this square root and we can neglect the Δz^2 term:

$$S = \frac{1}{2}\frac{R'}{R}\Delta z\frac{Y'^2}{R'^2} - \frac{1}{8}\frac{1}{R}\Delta z\frac{Y'^4}{R'^3} \tag{4.17}$$

considering only the first member and replacing $Y = D/2$ with D, the diameter of the pupil, we obtain:

$$S = \frac{1}{8}\Delta z\frac{D^2}{R^2} \tag{4.18}$$

Therefore, the calibration equation for the Defocus is obtained replacing S with $conv_{defocus}/\Delta c$ and $\frac{D^2}{R^2}$ with $\frac{1}{F^2_{number}}$.

The calibration equations for the Tip/Tilt are simpler to derive. In fact, we must consider two flat wavefront: first WF orthogonal with the optical axis, while second WF with a tilt inclination with respect to the first as in
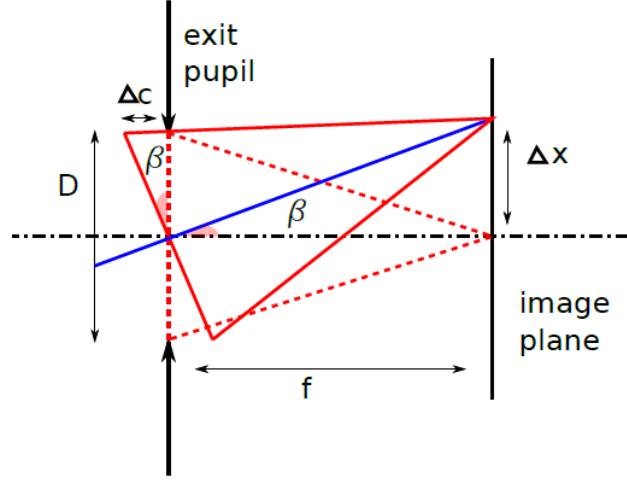
Figure 4.13: Scheme of the geometrical representation of the two flat wavefront. The dashed line orthogonal to optical axis, while the solid line tilted with respect to the optical axis.

figure 4.13. In this case, we can derive the calibration equation using only the geometric propriety of the system. In fact, we can write the following two equations:

$$\Delta c = \frac{D}{2} \sin \beta \tag{4.19}$$

$$\Delta x = f \sin \beta \tag{4.20}$$

where f is the focal length and D the diameter of the pupil. Getting $\sin(\beta)$ from the first equation and replacing in the second equation, we can obtain the two calibration equation for the Tip/Tilt.

Now the three equations for the calibration are:

$$S_{defocus} = \frac{1}{8} \cdot \left(\frac{1}{F_{number}} \right)^2 \cdot \frac{1}{m_{defocus}} \tag{4.21}$$

$$S_{tilt} = \frac{1}{F_{number}} \cdot \frac{1}{m_{tilt}} \tag{4.22}$$

$$S_{tip} = \frac{1}{F_{number}} \cdot \frac{1}{m_{tip}} \tag{4.23}$$

The angular coefficients m, defined as $\Delta c / \Delta(shift)$, are measured as variation of Zernike coefficient against the shift on one axis. This Zernike coefficient is obtained by mathematical equations as difference between the peak value and the valley value of the aberration. But, in this experiment, the

system measures the root-mean-square (RMS) of the Zernike polynomials. Therefore we have to multiply these equations by the constant values to restore them from peak-to-valley (PtV) to RMS values. The constant values are $1/4$ for the Tip/Tilt and $1/2\sqrt{3}$ for the Defocus.

4.1.4 SH-WFS arm opto-mechanical setup

To match the measures carried out with the P-WFS, we include in the system a SH-WFS in closed loop. A beam splitter cube, placed between the deformable lens and the first lens F_1, divides the incoming beam in two part. The first part goes on the closed loop with P-WFS, the second part is deflected in a secondary arm with SH-WFS (see Fig. 4.14).
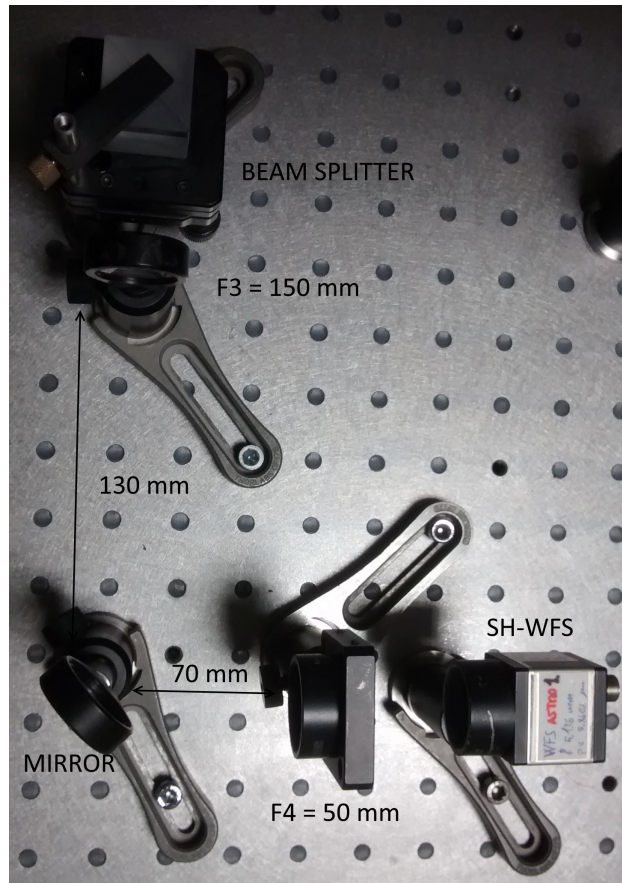

Figure 4.14: The image of the SH-WFS arm. We can notice the beam splitter, the two lenses F_3 and F_4 with focal length respectively of 150 and 50 mm. Finally, there is the SH-WFS in a conjugate plane with the DL.

In this secondary path there is two lenses with focal length of $F_3 = 150$ mm and $F_4 = 50$ mm. They are separated by the sum of their focal length, so they reduce the incoming collimate beam having diameter of 10 mm into an exit collimate beam having diameter of 3 mm. After this couple of lenses, the SH-WFS is located, that has the micro-lenses array of 6 mm of diameter (see Fig. 4.15).
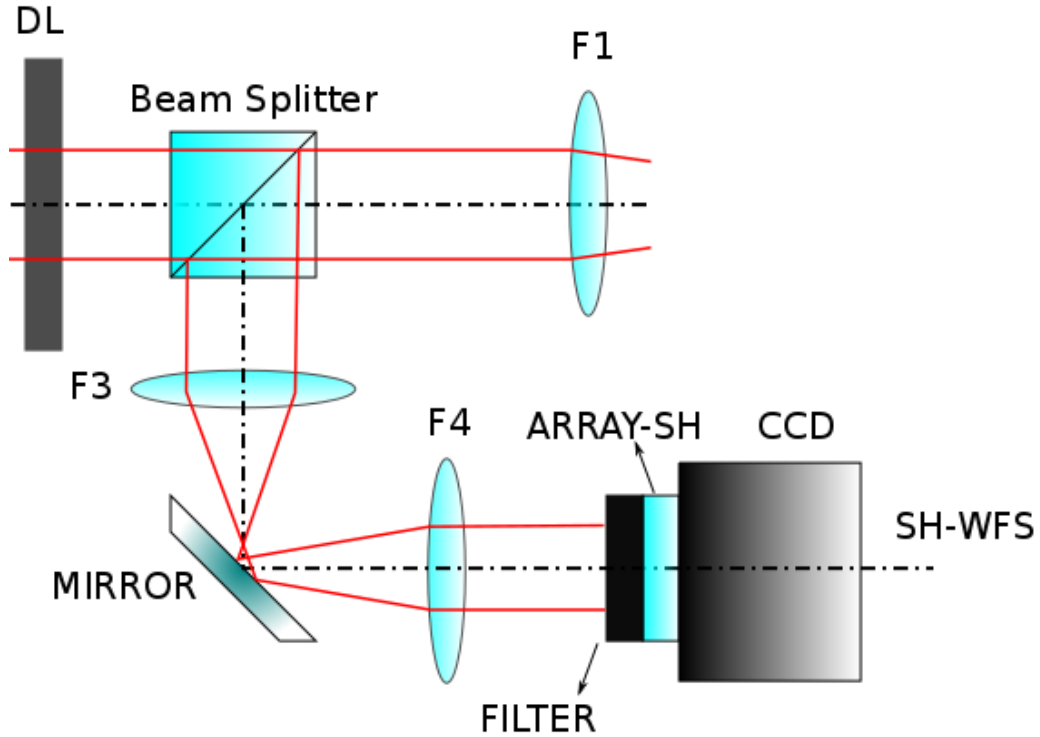

Figure 4.15: Scheme of the SH-WFS arm in closed loop. Following the optical path of the SH-WFS, there are: the DL, the beam splitter, the lenses F_3 and F_4 separated by the sum of the focal length and finally the SH-WFS conjugate with the DL.

The micro-lenses array of SH-WFS is conjugate with the same DL and a $NGG11$ filter with transmission of 0.1% is placed in front of the SH-WFS to reduce the intensity of the laser beam. The SH-WFS used has just assembled (Mocci, 2018, [33]). In fact, it is composed of an array with $40x40$ micro-lenses having diameter 150 micron. This array is fixed to a CCD at distance of its focal length (5.139 mm). Furthermore the array is aligned to the surface of the CCD that has a pixel size of 5.86 micron and a resolution of $1936x1216$ pixel. In this case, the software to use the SH-WFS has just implemented, it is $PhotonLoop$ developed by Jacopo Mocci (Mocci, [33]).

4.2 Data acquisition

Now the system is ready to acquire and to correct the incoming wavefront. This Section studies the stability of the system, in particular, the stability of the P-WFS to measure the same static aberrations and the stability of the DL to maintain the same shape over time. Finally, this Chapter concludes with the measurement of the NCPA of the system and with the stability of the DL to correct them over time.

4.2.1 Stability of the P-WFS

An important feature of the AO system is the stability over time. In particular, being in static case, the aberrations of non common path are produced by the optical element of the system and they must be constant over time. To check the stability of the P-WFS arm, we measure the values of the RMS of the wavefront and the lower orders of the Zernike coefficients over a period of 30 minutes with the DL switched-off (see Fig. 4.19). We can observe small variations of these coefficients over time. These variations are induced by small perturbations of the medium that induce variations on aberrations of the wavefront. On the other side, we can notice that the measures taken have some noise. This noise is due to statistical errors produced by the vibrations and local turbulence.

To reduce such effects, we can try to isolate the optical system. A cover of cardboard is built as in figure 4.17. With this cover the P-WFS should be isolated from the perturbations produced by the movement of external sources. Then, we repeat the previous step to measure the improvements of the system with the cover over time (see Fig. 4.18).

Now we can compute the standard deviations of the coefficients measured to estimate the noise error introduced by external factors. The values are reported in the following table 4.1:

RMS	Tilt Y	Tilt X	Ast Y	Def	Ast X
0.0058	0.009	0.007	0.0006	0.003	0.001
0.0023	0.006	0.005	0.0005	0.002	0.0007

Table 4.1: Standard deviation of the RMS and the first five Zernike modes (in waves) without cardboard cover in the first row and with the cardboard cover in the second row. The other four Zernike modes plotted in the figure 4.18 have the same standard deviation.
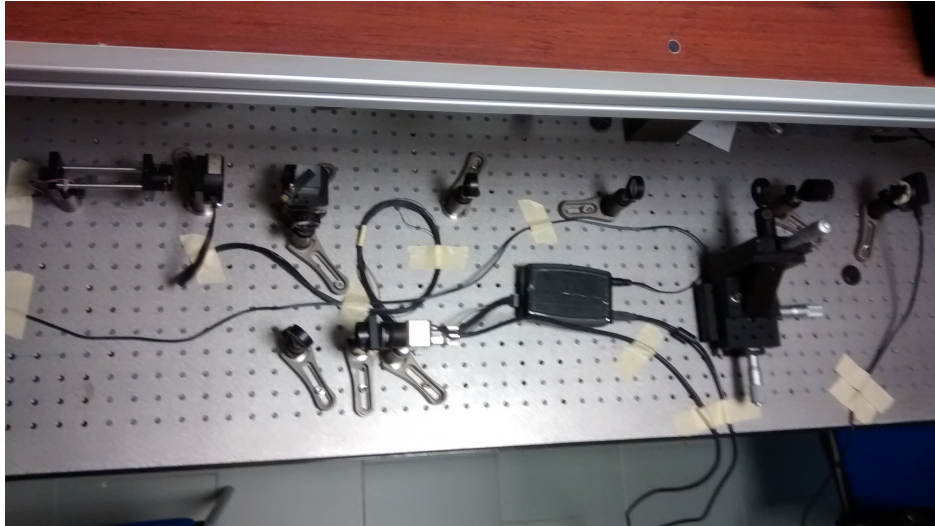
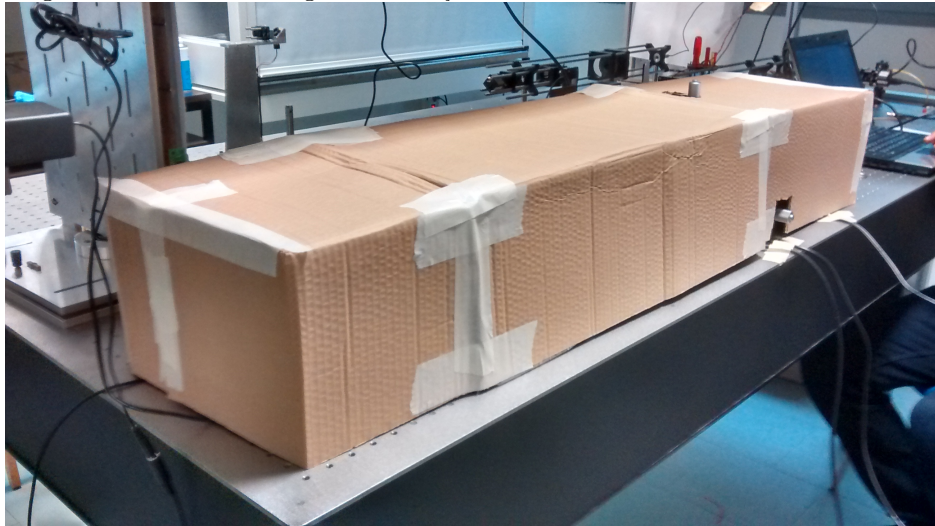Figure 4.16: The image of the system without the cardboard cover.

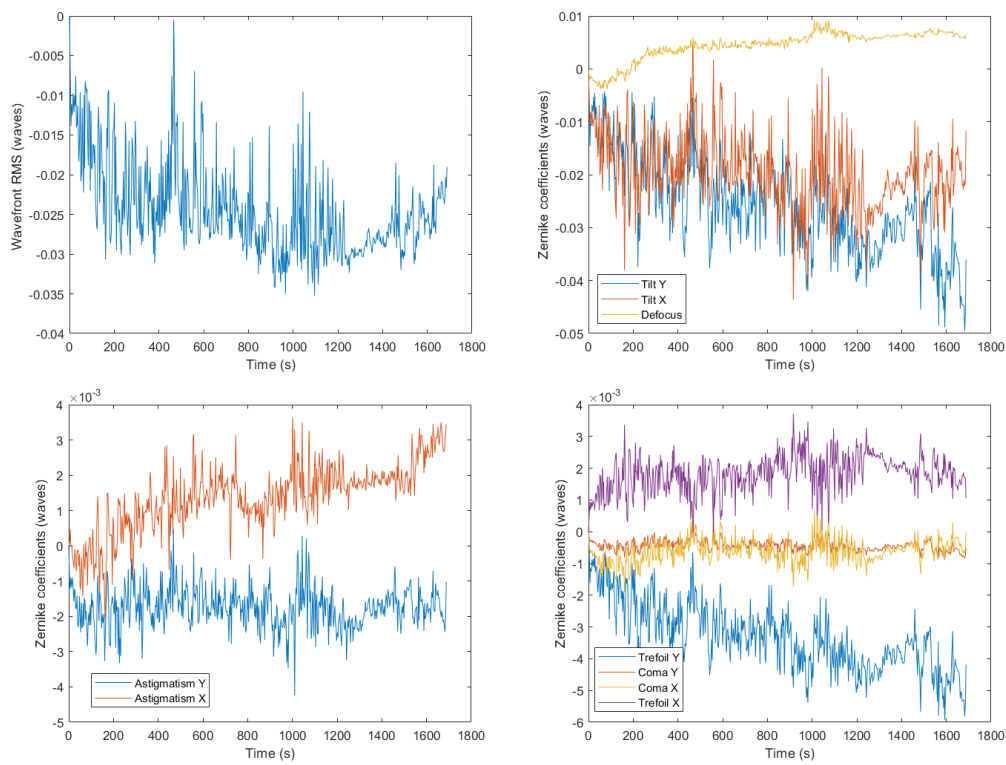Figure 4.17: The image of the optical system with the cardboard cover.

Figure 4.18: Plots of the P-WFS stability to measure the wavefront aberrations with the cardboard cover. In particular, the variations of the wavefront RMS and the first 10 Zernike coefficients for 25 minutes.

Observing the difference between the data taken with cover and the data taken without the cover, we can observe that in the first case the noise on the RMS is smaller by a factor 2.5. In particular, the RMS noise, when the cardboard cover is placed, becomes lesser than the residual RMS due to the correction of the P-WFS in closed loop (0.005 waves). Moreover the Tip/Tilt noise, induced by small turbulence in the air, is reduced. In fact, the cardboard cover not only limits the air turbulence nearly the optical system, but it protects the system from turbulence motions due to the movements of the bodies inside the room. Excluding the Tip/Tilt aberrations, the P-WFS measures the same aberrations over time. For these reasons, we go on the experiment with the cardboard cover.
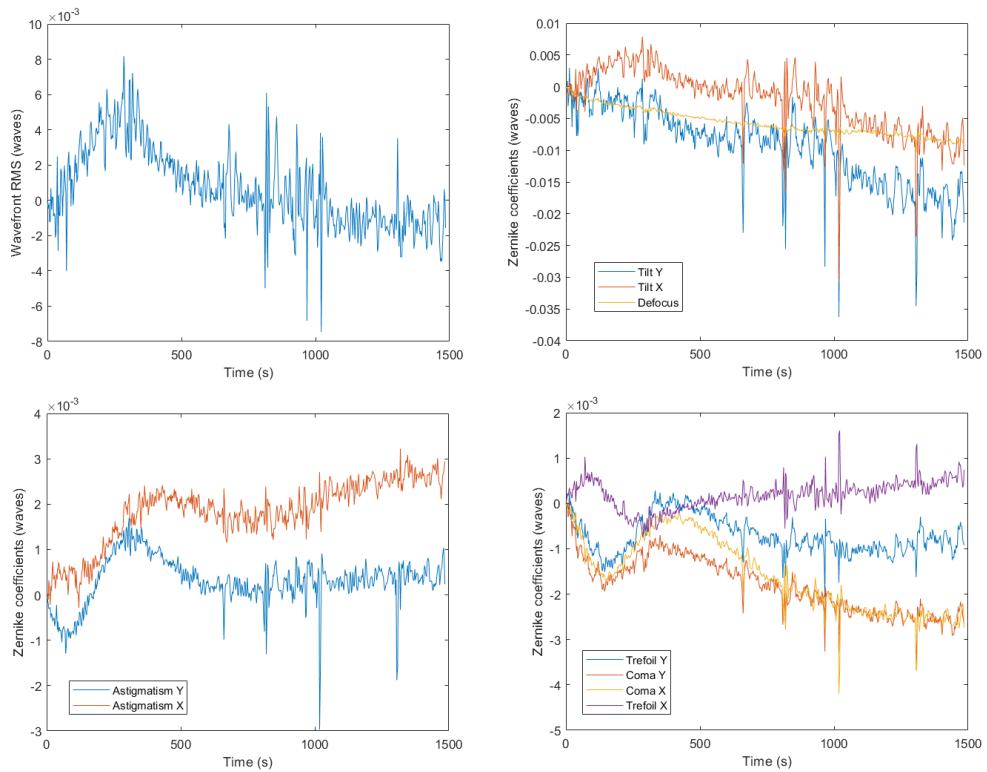

Figure 4.19: Plots of the P-WFS stability to measure the wavefront aberrations. In particular, the variations of the wavefront RMS and the first 10 Zernike coefficients for 30 minutes.

4.2.2 NCPA of the system

Now that we have just demonstrated the stability of the system to measure the aberrations over time, we can measure the NCPA between the two WFSs. In particular, when the optics of the system is not perfectly aligned and when they have some defects, the sensor of AO measures the aberrations induced by these components. These aberrations are different when the light travels different optical paths, for example the WFS arm and the scientific camera arm. The difference of the aberrations between the different optical paths is the non common path aberrations.

The aim of the experiment is to show that, by inserting a DL in the WFS arm, it is possible to compensate the NCPA with respect to the scientific arm bringing the P-WFS back to the optimal regime. In this case the deformable optical elements are two: the first element is the primary deformable mirror used to eliminate the turbulence aberrations, and the second element is a deformable lens placed after the beam splitter of the system that can be a deformable lens used to eliminate the NCPA (see Fig. 4.20).

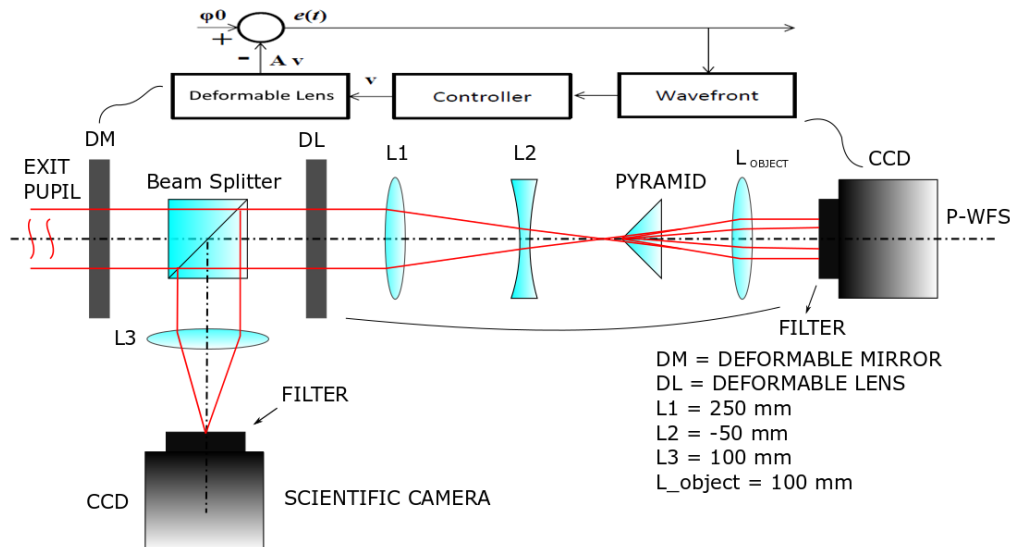Figure 4.20: Scheme of an AO system with P-WFS in closed loop with a deformable mirror. The NCPA are removed by a deformable lens, placed in the WFS arm, in open loop with the P-WFS.

For this test only a DL was available, so that we put it before the beam splitter. In this way, we can observe and measure the difference of aberrations between the two arms and the relative improvement when the DL eliminate them (see Fig. 4.1).

To calculate the deformation to send to the deformable lens to correct the non common path aberrations, we can use two methods. The first method uses the SH-WFS in closed loop with the deformable lens to deform it by varying the Zernike modes. At the same time the P-WFS measures the aberrations of the wavefront and the variance of the intensity inside the four pupil. The variance of intensity has been defined as the value of the squared deviation from the mean intensity inside the four pupils. Minimizing the variance of intensity, the four pupils tend to be uniform in intensity and so the wavefront tends to be flat. When the values of the RMS and of the variance of intensity are minimize, the actuators of the lens have the best values to correct the NCPA.

To do this, we change the offset of the Zernike modes on SH-WFS in closed loop in two steps. In the first step, we change the Zernike modes of 0.05 waves at a time by commanding DL (see Fig. 4.21). We save the best offset in SH-WFS, then we repeat this step changing the Zernike modes of 0.01 waves at time with respect to the previous offset (see Fig. 4.22). These plots show the variation of the RMS and of the variance of intensity measured with P-WFS against the variation of the offset of the Zernike modes in the SH-WFS in closed loop with deformable lens.

After these steps, the best offset of Zernike modes to correct the non common path aberrations is that in the following table 4.2, where the units are waves.

Ast Y	Defocus	Ast X	Tref Y	Coma Y	Coma X	Tref X
-0.03	-0.05	0.06	0.03	0.0	0.0	0.02

Table 4.2: Table of the NCPA values measured by the P-WFS while the SH-WFS is in closed loop with DL (values in waves).

The second method to evaluate the best offset is the P-WFS in closed loop with the DL, while the SH-WFS measures the aberrations induced in the wavefront by the deformation of DL. In fact, P-WFS in closed loop corrects the non common path aberrations deforming the DL and these deformations are observed by the SH-WFS as the inverse of the non common path aberrations. In this way the best offset found is reported in the table 4.3.

The two results of the offset value to eliminate the non common path aberrations are practically the same inside the error. But, in the first case, the P-WFS measure a residual wavefront in RMS of 0.022 waves, while, in the second case, the P-WFS can achieve a residual wavefront in RMS of 0.005 waves. Therefore we use the second method to evaluate the non common

Ast Y	Defocus	Ast X	Tref Y	Coma Y	Coma X	Tref X
-0.03	-0.05	0.07	0.03	-0.01	-0.01	0.02

Table 4.3: Table of the inverse NCPA values measured by the SH-WFS while the P-WFS is in closed loop with DL (values in waves).
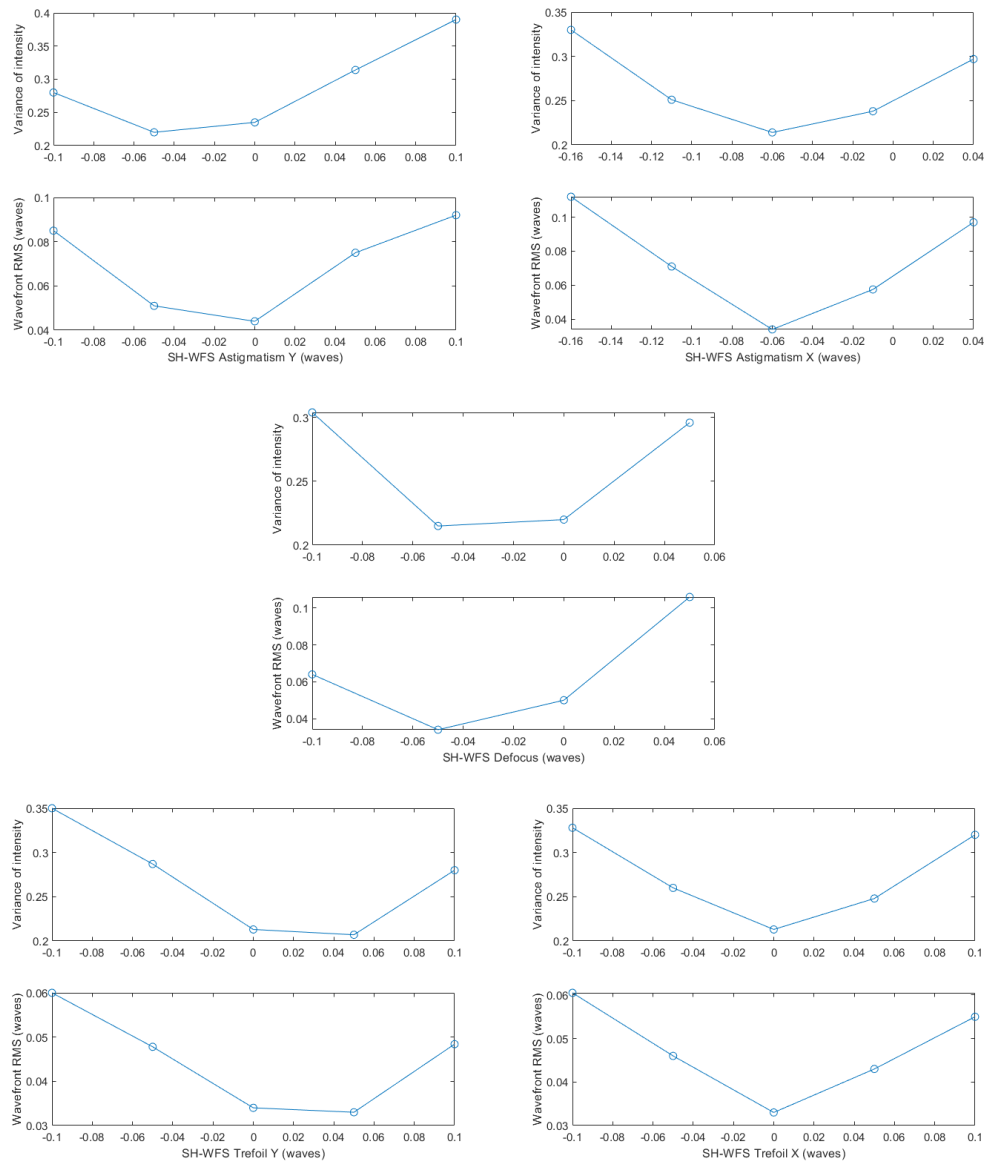

Figure 4.21: RMS and variance of intensity in the P-WFS against the offset of Zernike modes in the SH-WFS with 0.05 λ by step.
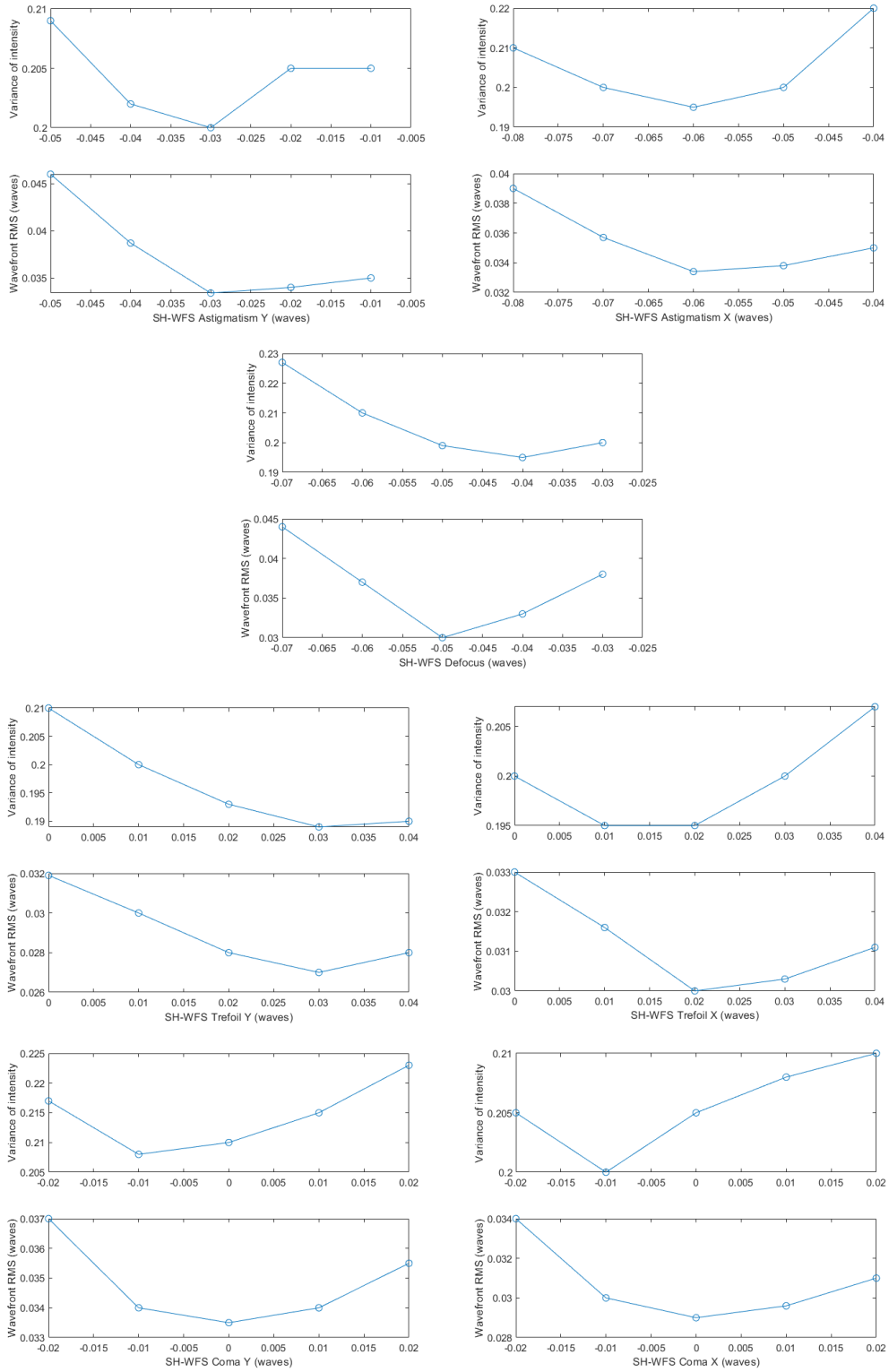
Figure 4.22: RMS and variance of intensity in the P-WFS against the offset of Zernike modes in the SH-WFS with 0.01 λ by step.

path aberrations in the following. Moreover, during this process we verify that the DL keeps, if we change the value of a Zernike mode, the others modes constant over time. Therefore, if we change a bit a Zernike mode maintaining the value inside the linear range, the increase of RMS measured by the P-WFS is due only to that Zernike mode. This fact is important to the next step where we change the value of one Zernike mode at time, without losing the corrections in the others Zernike modes. In this way the RMS of the wavefront, and also the Strehl ratio, do not change a lot.

Finally, having measured the NCPA, we show that the DL is able to correct these aberrations over time. To do this, the SH-WFS sends to the actuators of the DL an offset of commands to compensate the NCPA of the P-WFS arm. Then we measure the aberrations observed by the P-WFS and by the SH-WFS for 30 minutes without sending any other command to the DL. In this way, we simulate a system where the DL is in open loop with the P-WFS and it have to maintain the same shape during that AO system works. In my optical setup the P-WFS measures a flat wavefront due to the elimination of the aberrations by the DL (see Fig. 4.23), while the SH-WFS measures the NCPA in the same time (see Fig. 4.24). The figure 4.25 show the RMS values in waves both the P-WFS and the SH-WFS when the DL compensate the NCPA on the pyramid pin.
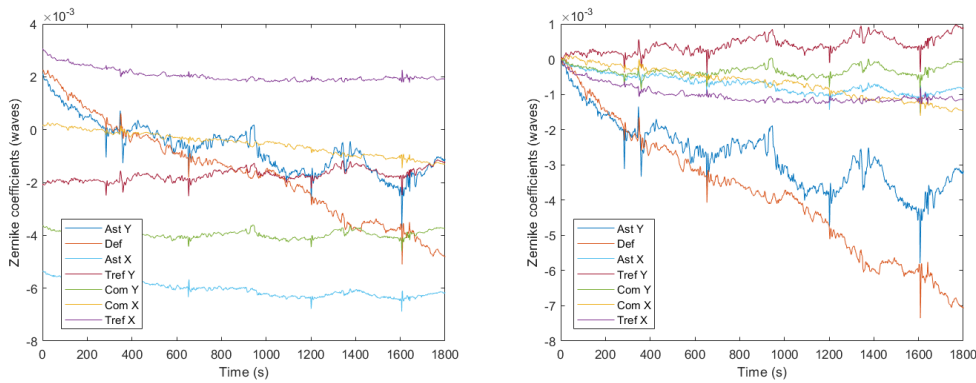
Figure 4.23: Plot of the aberrations measured by the P-WFS with DL that corrects the NCPA with a initial command input. On left the Zernike coefficients measured by the P-WFS; on right the variations of the Zernike coefficients in the same measurements.

From these two plots, we calculate the error (standard deviation) of the DL to maintain the same aberrations for 30 minutes as less than $5 \cdot 10^{-4}$ waves of residual RMS. In particular, this error is smaller of one order of magnitude than the residual RMS of the P-WFS to correct the wavefront
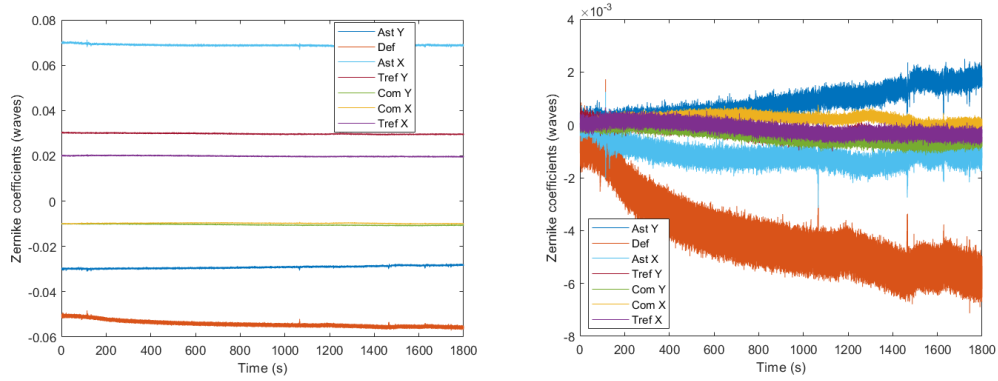
Figure 4.24: Plot of the NCPA measured by the SH-WFS over time, while the DL corrects the NCPA on the P-WFS. On left the Zernike coefficients (waves) measured by the SH-WFS; on right the variations of the Zernike coefficients (waves) in the same measurements.
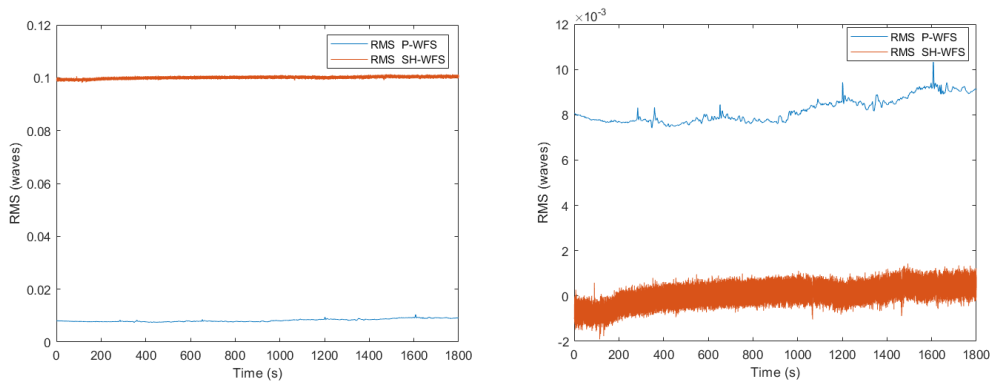

Figure 4.25: Plot of the wavefront RMS values (waves) measured by the P-WFS (in blue) and by the SH-WFS (in red). On left the RMS values of the two arms; on right the RMS variations of the two arms.

aberrations (0.005 waves). Therefore the DL can compensate the NCPA
of the system and it can maintain these corrections for long time without
any input. Obviously, the shape of the DL can more accurate in open loop
sending a constant input to the actuators to prevent the relaxing effects. In
particular, we can notice in figure 4.23 that only the Defocus mode has a
variation between the beginning and the end of the measurement of 0.006
waves. But the same variation is measured by the SH-WFS working in closed
loop (see Fig. 4.24). This error, however very small with respect to the error
of the P-WFS, on the Defocus mode is not related to the NCPA, but probably
it is due to the thermal error. In fact, during the operations of the system,
the components heat the system bringing a dilatation of the surrounding that
leads to a variation of the length of optical path. For this reason the Zernike
mode of Defocus is more affected by this process with respect to the other
Zernike modes.

Chapter 5

P-WFS gains and conclusions

In the previous Chapter we finally got the NCPA and the stability of the system to correct them. Now we can focus on the measures of the sensitivity gain and on the magnitude gain.

The P-WFS sensitivity changes with the aberrations of the wavefront and, therefore, with the Strehl ratio of the PSF on the pyramid pin. If the WF aberrations are reduced, the SR improves and consequently the P-WFS sensitivity increases. Thanks to this feature, the P-WFS becomes more efficient than the SH-WFS to correct the aberrations in closed loop. Moreover, the sensitivity gain can be used to improve the signal-to-noise of the measurements with a binning of the pixels in the P-WFS camera. In this way, the P-WFS improves its magnitude limit working in closed loop.

This Chapter focuses on the study of these features in two steps. First, we measure the sensitivity gain of the P-WFS changing the amplitude of the NCPA. Then, we use the theoretical magnitude gain of the P-WFS to derive the magnitude gain of this AO system without the NCPA. This Chapter concludes with the discussion about the usefulness of the DL in astronomy, in particular to compensate the NCPA in a P-WFS in closed loop.

5.1   Sensitivity gain in the experimental setup

The sensitivity gain of the P-WFS is due to the slope variation of the linear range in the S curve (see Fig. 3.8). In fact, the slope of the linear range of S curve is proportional to the sensitivity of the P-WFS. If the WF aberrations are removed, the extension of the linear range of S curve is reduced, but the P-WFS sensitivity increases with the slope of the linear range of S. This effect improves the P-WFS when this sensor works in closed loop.

In this Section, we fit the slopes of the S curves for each Zenike mode with and without the non common path aberrations. To get the S curves of the P-WFS, the procedure is similar to the calibration method previously explained (Section 4.1.3). In this case, we do not use the translator to induce a variation of the Zernike mode in the P-WFS, but we use the DL to produce the variation of the Zernike mode on the PSF in the pyramid pin. For this purpose, the DL is commanded by the SH-WFS. In this way, we can sample the S curves of the P-WFS for each Zernike mode of the second and third order. Furthermore we can compare the sensitivity of the P-WFS with the sensitivity of the SH-WFS. We do not sample the first order Tip/Tilt, but we remove these aberrations shifting the translator for every measurement to compensate the Tip/Tilt measured by the P-WFS.

The S curves of the P-WFS are extracted in two different conditions. The first condition happens when the SH-WFS corrects the aberration in closed loop with the DL and the P-WFS measures the NPCA (see Fig. 5.1). The second condition occurs when the SH-WFS sends to the DL the commands to remove the NCPA on the P-WFS arm. In both cases, we sample one Zernike coefficient at a time and the others remain fixed (see Fig. 5.2). In the first figure 5.1, the calibration coefficients are set for each Zernike mode. Therefore the P-WFS measures the same aberrations of the SH-WFS at the initial point of 0.73 SR. In the second figure 5.2, instead, the NCPA are eliminated by DL on the P-WFS arm, so they are measured by SH-WFS with the inverse sign. The difference between the two conditions is mainly on the increment of the slope values of the linear range when the NCPA are corrected bringing to an increment of the P-WFS sensitivity (see table 5.1).

Ast Y	Defocus	Ast X	Tref Y	Coma Y	Coma X	Tref X
1.17	1.42	1.81	1.66	1.29	1.29	1.38

Table 5.1: Table with the slopes of the linear ranges of the figure 5.2. The sensitivity for each Zernike mode is increased, in particular, stronger is the aberration on a Zernike mode and higher is the sensitivity gain of the P-WFS.

To extract the behavior of the P-WFS sensitivity with the variation of the NCPA, we repeat the previous procedure for four different non common path aberrations amplitudes. In particular, we extract the slopes of linearity curves with the overall NCPA, with 70 % of NCPA, with 30 % and without them. In this case, however, we change one Zernike mode at time but only for small value of 0.01 waves and without sampling the overall S curve but only a portion around the initial point (see Fig. 5.3).

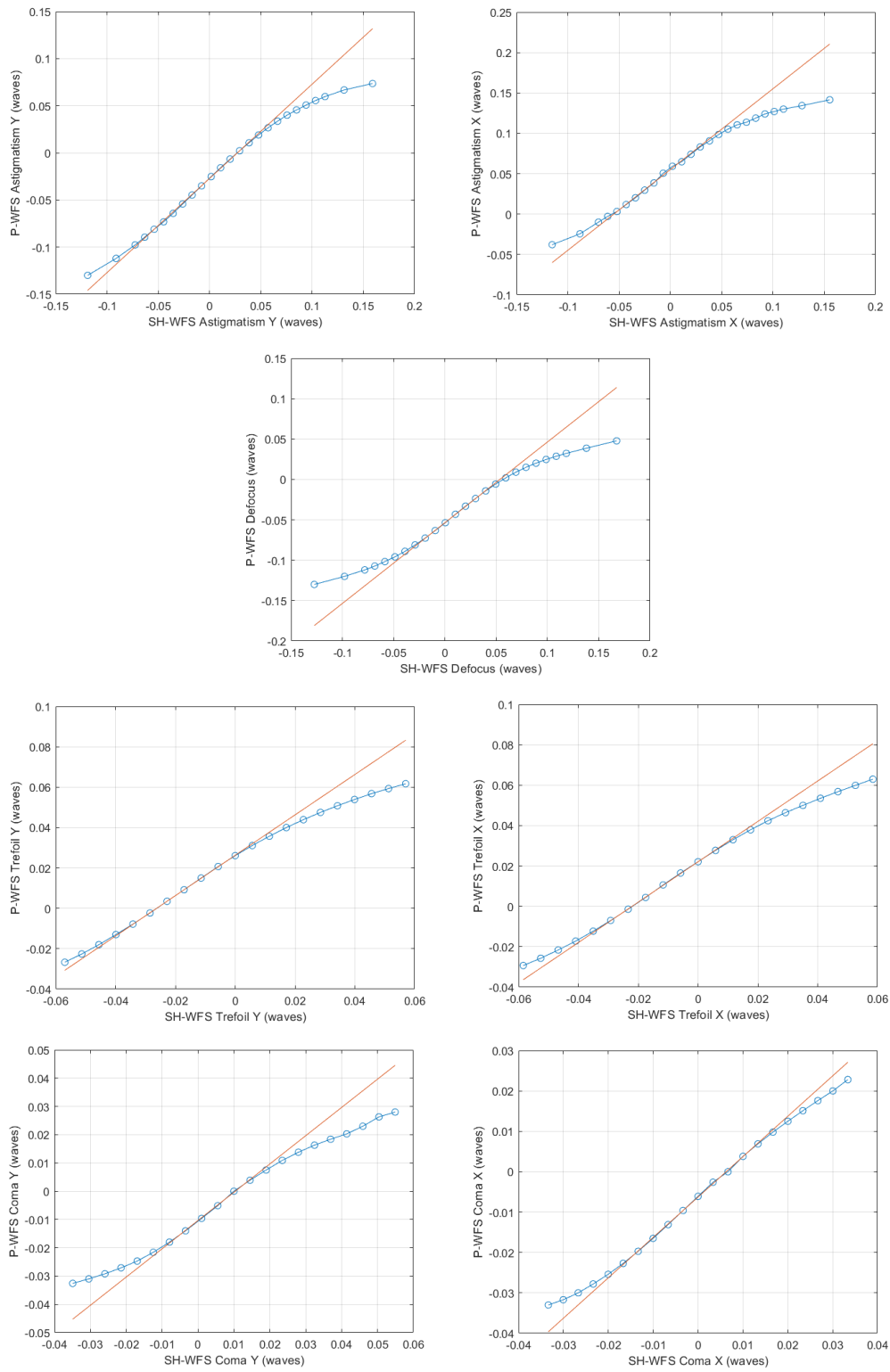Figure 5.1: The S curves for the Zernike modes up to the third order with the NCPA on the P-WFS arm. The calibration coefficients are set for each Zernike mode, so the slope of the linear range are equal to 1.

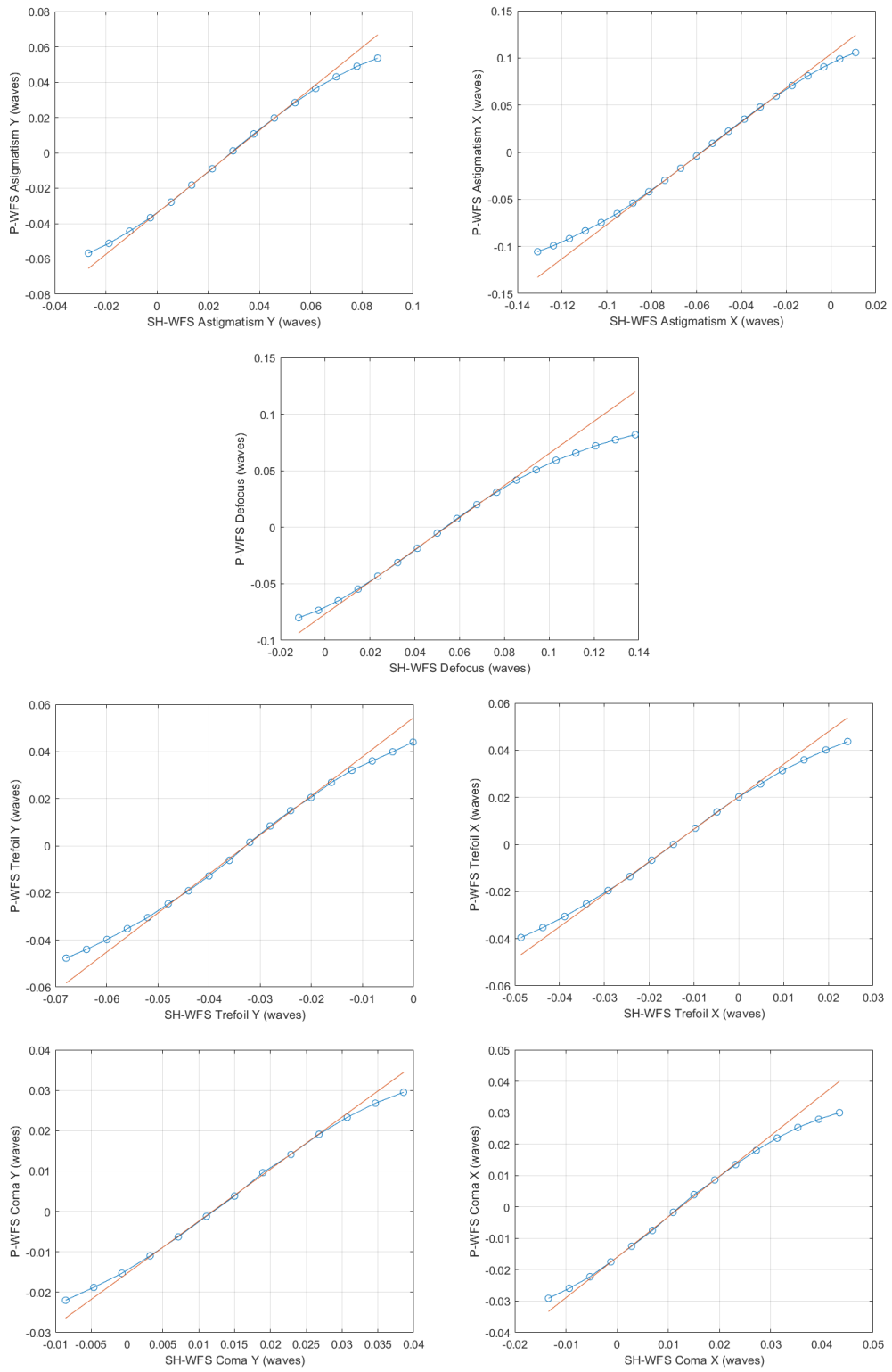Figure 5.2: The S curves for the Zernike mode up to the third order without the NCPA on the P-WFS. The slopes of the linear range for each Zernike mode are increased with respect the figure 5.1.
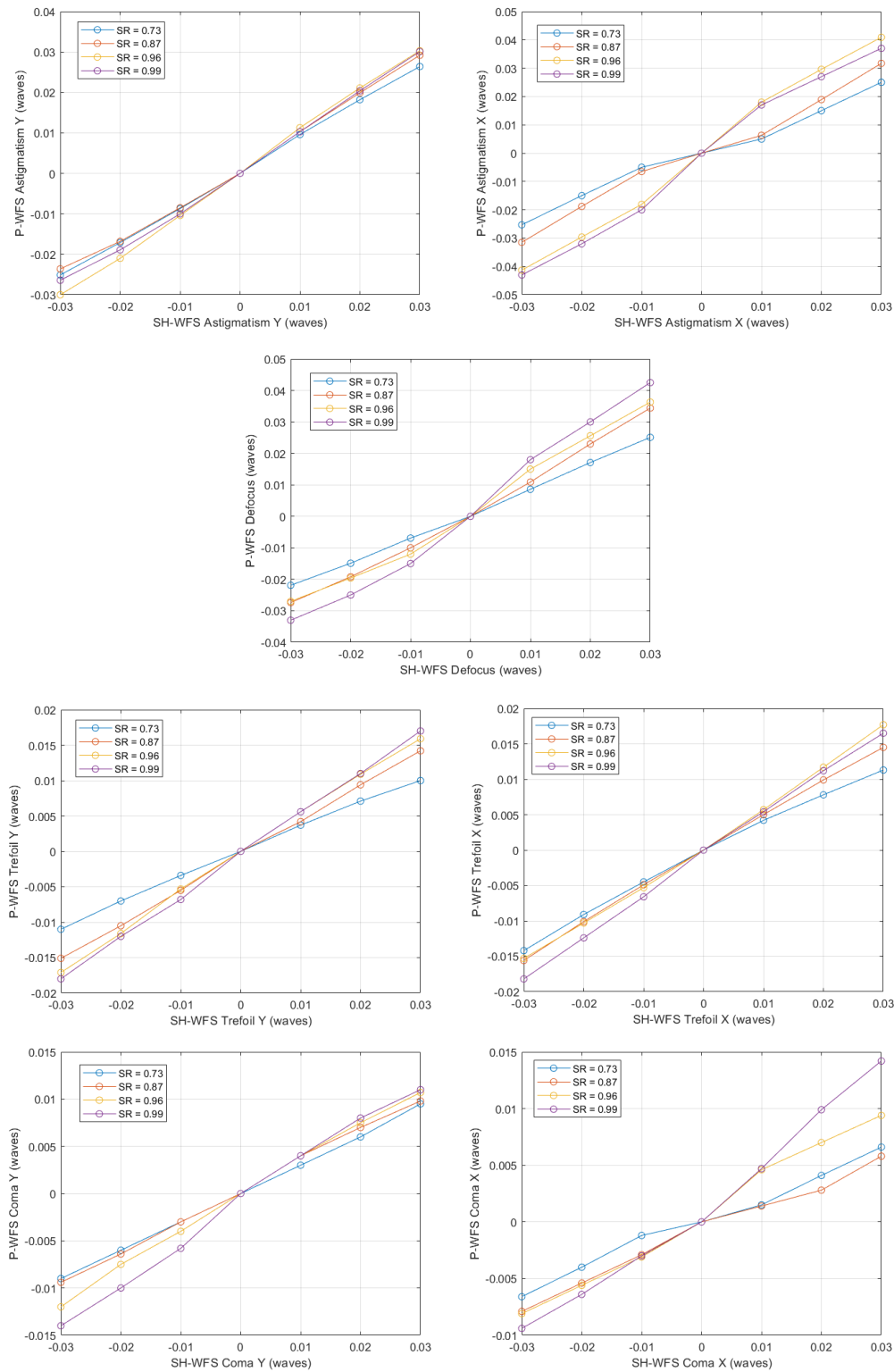
Figure 5.3: The linear range of the S curves for the Zernike modes up to the third order. The NCPA are changed for each curve, in particular, the SR of the P-WFS increases with the slope of the linear range for each Zernike mode.

RMS / SR		Astigmatism Y		Defocus		Astigmatism X	
NCPA	%	NCPA	sensitivity	NCPA	sensitivity	NCPA	sensitivity
0.1	73	0.03	1.00 ± 0.02	0.05	1.00 ± 0.04	0.07	1.00 ± 0.13
0.06	87	0.02	1.03 ± 0.07	0.03	1.2 ± 0.1	0.04	1.25 ± 0.16
0.03	96	0.01	1.10 ± 0.04	0.015	1.39 ± 0.17	0.02	1.78 ± 0.16
0.01	99	0.0	1.17 ± 0.06	0.0	1.42 ± 0.19	0.0	1.81 ± 0.22
Trefoil Y		Coma Y		Coma X		Trefoil X	
NCPA	sensitivity	NCPA	sensitivity	NCPA	sensitivity	NCPA	sensitivity
0.03	1.00 ± 0.04	0.01	1.00 ± 0.03	0.01	1.00 ± 0.08	0.02	1.00 ± 0.08
0.02	1.40 ± 0.04	0.005	1.06 ± 0.05	0.005	1.03 ± 0.09	0.01	1.19 ± 0.03
0.01	1.57 ± 0.05	0.0	1.23 ± 0.06	0.0	1.13 ± 0.10	0.005	1.31 ± 0.06
0.0	1.66 ± 0.05	0.0	1.29 ± 0.12	0.0	1.29 ± 0.16	0.0	1.38 ± 0.04

Table 5.2: The table of the sensitivity variations for each Zernike mode up to the third with relative NCPA value in waves. The sensitivity coefficients are equal to 1 for each Zernike mode in the initial condition of 0.73 SR.

The table 5.2 reports the values of the slopes, which represent the P-WFS sensitivity, with respect to the values of the NCPA in waves induced by the DL with the SH-WFS in closed loop.

As we can see in the table 5.2 the sensitivity of the P-WFS increases with the reduction of the non common path aberrations. In particular, stronger will be the corrected non common path aberration in a Zernike mode and greater will be the sensitivity gain.

5.2   Theoretical magnitude gain

The magnitude gain is presented by Ragazzoni (Ragazzoni, 1999, [34]), and by Viotto (Viotto, 2016, [13]). These articles describe the correlation between the sensitivity of P-WFS and the sensitivity of SH-WFS with respect to the Zernike radial order with which the AO system works. In particular, the aberrations of the atmospheric turbulence have an average Fried's parameter of r_0, and hence the maximum radial order that an AO system can correct is D/r_0, where D is the diameter of the telescope. Moreover, the number of actuators of the deformable element used in an AO system is proportional to $(D/r_0)^2$. These researches lead to the formulation of the theoretical magnitude gain depending on the ratio D/r_0 and on the SR of the PSF on the pyramid pin. This formulation, that we do not treat in the

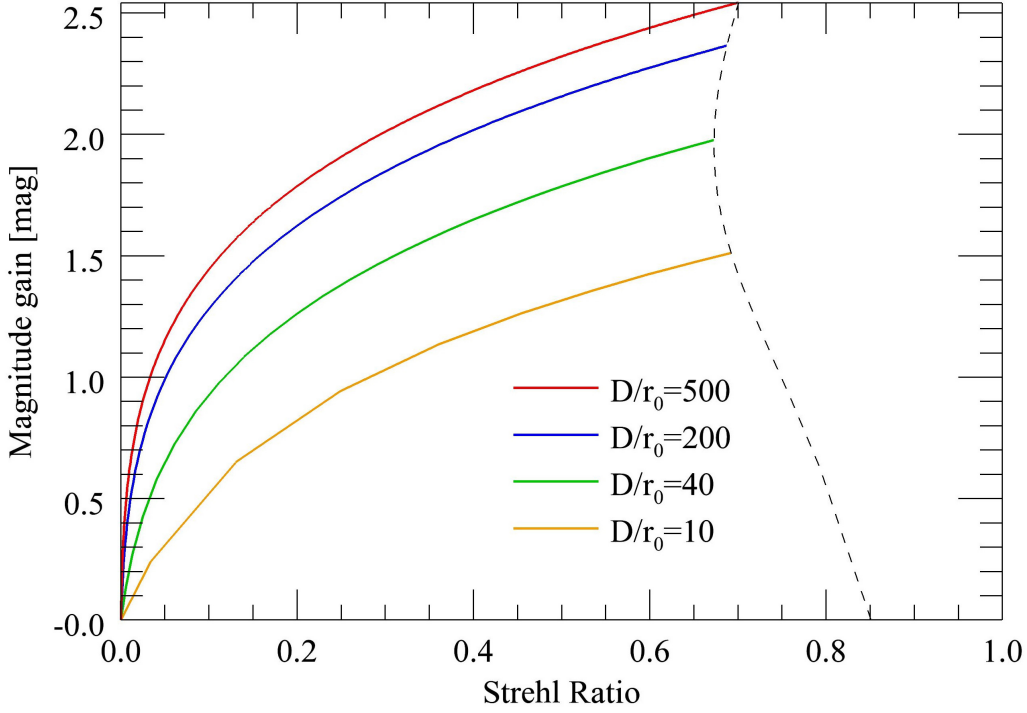specific, leads to the following plot (see Fig. 5.4):

Figure 5.4: Example of theoretical plot of the magnitude gain against the Strehl ratio from Viotto 2016. Four curves are reported for different ratios of D/r_0.

where the magnitude gain of the P-WFS depends on the SR of the wavefront and on the ratio D/r_0. Therefore, fixed the ratio D/r_0, the magnitude gain of the P-WFS increases in logarithmic with respect to the increment of the Strehl ratio. As we see in figure 5.4, the four curves are limited by the SR. This effect is due to the Marechal's approximation that calculates the maximum SR achieved by AO system with a fixed D/r_0 and after the correction of the first J Zernike modes. The Marechal's approximation is the following:

$$SR_J \approx exp(-0.2944J^{\sqrt{3}/2}(D/r_0)^{5/3}) \tag{5.1}$$

This limit in Strehl ratio is close to 70% in this example (Viotto, 2016, [13]).

Now we can use the figure 5.4 to estimate the magnitude gain due to the elimination of the NPCA by a DL in open loop on the P-WFS arm. We start considering a typical telescope as the $VLT\,UT1$ of the ESO (European Southern Observatory) in Chile with a diameter of $D = 8.2$ meter. If we take the Fried's parameter around $r_0 \approx 0.20$ meter, we select the curve relative to

the ratio $D/r_0 = 40$. In this case, the overall aberrations, measured by the P-WFS before starting the closed loop, are composed of the aberrations of the turbulence plus the NCPA. This effect leads difficulty to close the loop with the P-WFS due to low SR of the PSF. In fact, strong aberrations lead to saturate the S curve of the P-WFS. For example, if the initial SR in the pyramid pin is 0.2, we can calculate the SR of the same system in the same condition without NCPA. In this experiment, we have measured a NCPA amplitude in RMS of 0.1 waves. Therefore, we can estimate the SR of the system without the NPCA using the following equation:

$$SR = exp[-(2\pi RMS)^2] \tag{5.2}$$

This equation can be inverted to obtain the RMS equal to $SR = 0.2$, then we subtract the RMS due to the NCPA (0.1 waves) and finally we re-calculate the new SR of the system without the NCPA. In this example, the new SR of the system is 0.65. Now we can observe directly the magnitude gain of the P-WFS at the beginning of the closed loop without the NCPA as in the following figure 5.5:
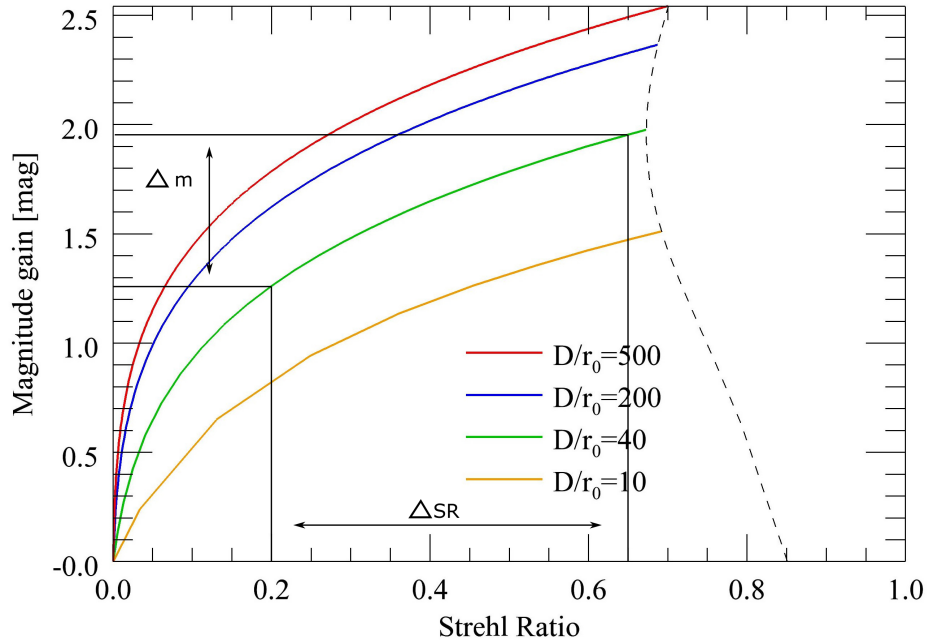

Figure 5.5: Example of theoretical plot of the magnitude gain against the Strehl ratio from Viotto 2016. An example of magnitude gain for a system with $D/r_0 = 40$, initial $SR = 0.2$ with NCPA and initial $SR = 0.65$ without NCPA.

The magnitude gain valued is 0.7 *mag*. This great improvement can be calculated for any initial SR and for any value of D/r_0.

5.3 Conclusions

The non common path aberrations limit a real AO instrument based on the P-WFS in closed loop. In fact, in an AO system in closed loop, the incoming photon beam captured by the telescope reaches a beam splitter after the deformable element. The wavefront is divided along two arms: the first WF is led to the P-WFS to correct the aberrations measured, the second WF is led to the scientific camera. Therefore the wavefront incoming from the star travels the last part through two different optical paths, that add different static aberrations in the wavefront. This effect brings the creation of non common path aberrations between the two arms. Such NCPA limit the sensitivity of the P-WFS or, alternatively, the SR in the scientific camera. Moreover, they contribute to saturate the S curve of the P-WFS.

That issue can be dealt in three different methods:

1. in the first method, we can consider the NCPA very small. In this way, the P-WFS corrects the wavefront aberrations and the P-WFS sensitivity of the AO system improves up to maximum value. In this case, the scientific camera measures a static deformation of the WF due to the NCPA. Therefore the PSF on the scientific camera does not achieve the diffraction limit. This method is useful if the NCPA between the two arms of the system are negligible;

2. in the second method, alternatively, the P-WFS can add the opposite NCPA to the primary deformable element to compensate the NCPA on the scientific camera arm. In this way, the P-WFS takes into account the NCPA during the correction, and so the PSF on the scientific camera tends to diffraction limit. On the other side, the PSF on the pyramid pin is affected by the NCPA bringing the sensor out of the optimal regime. This method limits the sensitivity gain and the magnitude gain of the P-WFS. This method is useful if we have a bright reference source or if we do not need a deeper sampling of the turbulence;

3. in the last method, we use a deformable element in the P-WFS arm. In this case we can set the wavefront contribution of the deformable element as the opposite of the NCPA. Therefore the deformable element eliminates the NCPA in the P-WFS without introducing any aberrations in the scientific camera. In this way we can have the PSF in diffraction limit both on the P-WFS and on the scientific camera.

This thesis focuses on the third method presented, in particular, the DL can be used to reduce the NCPA in P-WFS arm below 0.01 waves RMS (see Fig. 4.25). In addition we measured that the DL correction can be maintained with a stability of about 0.001 waves RMS over periods of 30 minutes. This feature allows to increase the sensitivity of the P-WFS until the maximum value, keeping the PSF on the scientific camera to the diffraction limit.

Finally, we summarize the main features of the components used in the experiment and the results achieved:

1. the deformable lens is a new innovative deformable optical element that allows to correct up to the 4th order of Zernike modes with performances comparable to deformable mirrors. The use of a DL instead of a deformable mirror allows the implementation of adaptive optics setups on existing systems without major redesign (Section 3.1.1);

2. the P-WFS sensitivity improves during the correction of the aberrations in closed loop. Alternatively, the sensitivity can be reduced with a binning of CCD pixels that enlarges the sub-apertures to sample the wavefront. Instead, the sensitivity of the SH-WFS is fixed and it depends on the size and on focal length of the micro-lenses (Section 3.2);

3. a AO system in closed loop might be affected by NCPA. In particular, the difference of the optical paths between the WFS arm and the scientific camera arm brings to arise a static aberrations. These aberrations influence the system typically on the lowest Zernike modes. The NPCA, in a AO system with P-WFS in closed loop, affect the scientific camera reducing the PSF in the image, or, alternatively, they affect the PSF in the pyramid if a bias is inserted in the control system (Section 4.2.2);

4. we can eliminate the NCPA in the AO system by placing a DL in the P-WFS arm with this deformable element. In this way, the P-WFS sensitivity improves to the maximum value and the PSF in the scientific camera reaches the diffraction limit. Therefore, the P-WFS can measure the aberrations of the wavefront with deeper sampling than the SH-WFS (Section 5.1);

5. we can use the sensitivity gain of the P-WFS to improve the magnitude limit of the AO system. In fact, binning the pixels of the P-WFS camera, the sub-apertures of the WFS get bigger and the sensitivity of the pyramid decreasing. In this way, the signal-to-noise of the measurement of the wavefront improves, and so the P-WFS can use a fainter

source to estimate the aberrations. This feature allows to increase the sky coverage of the reference source to the P-WFS (Section 5.2);

6. the compensation of the NCPA in the P-WFS arm can be done by any deformable optical element. However, only the DL is able to correct them without changing the system size. In fact, on the opposite of deformable mirrors, the DL can be placed inside the optical setup without modifying the optical arrangement.

In this thesis we have demonstrated that an adaptive lens is an effective and convenient device for the correction of the NCPA for large telescopes to reach their maximum resolution.

Bibliography

[1] R. K. Tyson, "Introduction to adaptive optics," *SPIE Publications*, vol. TT41, p. 121, 2001.

[2] S. Bonora, Y. Jian, P. Zhang, A. Zam, E. N. Pugh, R. J. Zawadzki, and M. V. Sarunic, "Wavefront correction and high-resolution in vivo oct imaging with an objective integrated multi-actuator adaptive lens," *Optics Express*, p. 11, 2015.

[3] J. W. Hardy, "Adaptive optics for astronomical telescopes," *Oxford University Press*, p. 448, July 1998.

[4] C. Vérinaud, M. Le Louarn, V. Korkiakoski, and M. Carbillet, "Adaptive optics for high-contrast imaging: Pyramid sensor versus spatially filtered shack-hartmann sensor," *Monthly Notices of the Royal Astronomical Society: Letters*, p. 5, 2005.

[5] R. Ragazzoni, "Pupil plane wavefront sensing with an oscillating prism," *Journal of Modern Optics*, vol. 43, pp. 289–293, Feb. 1996.

[6] R. Ragazzoni, E. Diolaiti, and E. Vernet, "A pyramid wavefront sensor with no dynamic modulation," *Optics Communications*, vol. 208, pp. 51–60, July 2002.

[7] J. H. Lee, "Pupil plane wavefront sensing with a static pyramidal prism: simulation and preliminary evaluation," *Journal of the Optical Society of Korea*, p. 6, 2000.

[8] C. Vérinaud, C. Arcidiacono, M. Carbillet, E. Diolaiti, R. Ragazzoni, E. Vernet-Viard, and S. Esposito, "Layer oriented multi-conjugate adaptive optics systems: performance analysis by numerical simulations," *Proceedings of SPIE*, vol. 4839, pp. 524–535, Feb. 2003.

[9] M. Le Louarn, C. Verinaud, and V. Korkiakoski, "Simulation of mcao on (extremely) large telescopes," *Comptes Rendus Physique*, vol. 6, pp. 1070–1080, Dec. 2005.

[10] R. Ragazzoni, A. Ghedina, A. Baruffolo, E. Marchetti, J. Farinato, T. Niero, G. Crimi, and M. Ghigo, "Testing the pyramid wavefront sensor on the sky," *Proceedings of SPIE*, pp. 423–430, 2000.

[11] S. Wang, C. Rao, H. Xian, J. Zhang, J. Wang, and Z. Liu, "Laboratory demonstrations on a pyramid wavefront sensor without modulation for closed-loop adaptive optics system," *Optics Express*, p. 16, 2011.

[12] Y. Liu, Q. Mu, Z. Cao, L. Hu, C. Yang, and L. Xuan, "Precise calibration of pupil images in pyramid wavefront sensor," *Applied Optics*, vol. 56, pp. 3281–3286, Apr. 2017.

[13] V. Viotto, R. Ragazzoni, M. Bergomi, D. Magrin, and J. Farinato, "Expected gain in the pyramid wavefront sensor with limited strehl ratio," *Astronomy and Astrophysics*, vol. 593, p. A100, Sept. 2016.

[14] J. Cheng, "The principles of astronomical telescope design," *Astrophysics and Space Science Library*, vol. 360, p. 642, 2009.

[15] T. S. McKechnie, "General theory of light propagation and imaging through the atmosphere," *Springer Series in Optical Sciences*, vol. 169, p. 639, 2016.

[16] F. Roddier, "The effects of atmospheric turbulence in optical astronomy," *Progress in Optics*, p. 96, 1981.

[17] S. S. Zilitinkevich, T. Elperin, N. Kleeorin, I. Rogachevskii, I. Esau, T. Mauritsen, and M. W. Miles, "Turbulence energetics in stably stratified geophysical flows: Strong and weak mixing regimes," *Quarterly Journal of the Royal Meteorological Society*, vol. 134, pp. 793–799, Apr. 2008.

[18] T. Morris, "Tomographic adaptive optics and turbulence profiling," *Journal of Physics Conference Series*, vol. 595, pp. 012–021, Apr. 2015.

[19] R. K. Tyson and W. F. Benjamin, "Field guide to adptive optics," *SPIE Field Guides*, vol. FG24, p. 140, 2012.

[20] V. Viotto, "Adaptive optics bites," *University of Padua*, p. 41, 2012.

[21] J. C. Wyant, "Zernike polynomials," *ZernikePolynomialsForWeb*, pp. 1–29, 2003.

[22] L. N. Thibos, R. A. Applegate, J. T. Schwiegerling, and R. Webb, "Standards for reporting the optical aberrations of eyes," *Journal of refractive surgery*, vol. 18, pp. S652–S660, 2000.

[23] D. F. Edwards, "Adaptive optics engineering handbook, by robert k. tyson," *Optics & Photonics News*, vol. 11, p. 46, Nov. 2000.

[24] V. Korkiakoski, "Improving the performance of adaptive optics systems with optimized control methods," *Teknillinen korkeakoulu*, p. 145, 2008.

[25] J. M. Le Due, "A study of the pyramid sensor: analytic theory, simulation and experiment," *Dalhousie University, University of Victoria*, p. 194, 2002.

[26] O. Martin, S. Turbide, F. Legace, F. Levesque, G. Anctil, F. Chateauneuf, D. Grousseau, W. Deschênes, and J.-P. Véran, "Ino pyramidal wavefront sensor demonstrator: first closed-loop on-sky operation at mont-mégantic telescope," *Adaptive Optics for Extremely Large Telescopes IV (AO4ELT4)*, p. E38, Oct. 2015.

[27] E. Dalimier and C. Dainty, "Comparative analysis of deformable mirrors for ocular adaptive optics," *Optics Express*, vol. 13, p. 4275, May 2005.

[28] R. J. Noll, "Zernike polynomials and atmospheric turbulence," *Journal of the Optical Society of America*, 1976.

[29] I. Mochi and K. A. Goldberg, "Modal wavefront reconstruction from its gradient," *Applied Optics*, vol. 54, pp. 3780–3785, 2015.

[30] D. Ramos-Lopez, M. A. Sanchez-Granero, M. Fernandez-Martinez, and A. Martinez-Finkelshtein, "Optimal sampling patterns for zernike polynomials," *Applied Mathematics and Computation*, p. 21, 2016.

[31] V. Akondi, B. Vohnsen, and S. Marcos, "Virtual pyramid wavefront sensor for phase unwrapping," *Applied Optics*, vol. 55, p. 8363, Oct. 2016.

[32] J. C. Wyant and K. Creath, "Basic wavefront aberration theory for optical metrology," *Applied Optics and Optical Engineering, Volume XI*, vol. 11, p. 2, 1992.

[33] J. Mocci, M. Quintavalla, R. Muradore, and S. Bonora, "Development of a cpu-based architecture for high performance adaptive optics systems," *IEEE Transactions on Industrial Informatics*, pp. 1–7, Jan. 2018.

[34] R. Ragazzoni and J. Farinato, "Sensitivity of a pyramidic wave front sensor in closed loop adaptive optics," *Astronomy and Astrophysics*, vol. 350, pp. L23–L26, Oct. 1999.

[35] S. M. Ammons, L. Johnson, E. A. Laag, R. Kupke, D. T. Gavel, B. J. Baumann, and C. E. Max, "Integrated laboratory demonstrations of multi-object adaptive optics on a simulated 10-meter telescope at visible wavelengths," *Publications of the Astronomical Society of the Pacific*, p. 29, 2009.

[36] J. Antichi, M. Munari, D. Magrin, and A. Riccardi, "Modeling pyramidal sensors in ray-tracing software by a suitable user-defined surface," *The Astronomical Journal*, p. 8, 2015.

[37] S. Esposito and A. Riccardi, "Pyramid wavefront sensor behavior in partial correction adaptive optic systems," *Astronomy and Astrophysics*, vol. 369, pp. L9–L12, Apr. 2001.

[38] F. Rigaut and E. Gendron, "Laser guide star in adaptive optics - the tilt determination problem," *Astronomy and Astrophysics*, vol. 261, pp. 677–684, Aug. 1992.

[39] A. Tokovinin, "Where is the surface-layer turbulence?," *Proceedings of SPIE*, vol. 7733, p. 77331N, July 2010.